Construction of Polymer Ultrathin Films with Nanostructures as a Model for Biological Soft Matter Systems

A Thesis

Presented to

Waseda University

July 2012

Hong ZHANG

Promoter: Prof. Dr. Shinji Takeoka

Referees: Prof. Dr. Yasuo Ikeda

Prof. Dr. Nobuhito Goda

Prof. Dr. Shin'ichi Ishiwata

Preface

Soft matter is a material that displays solid-like properties but is distinct from traditional materials in that it is more deformable and liquid-like. A number of biosystems are classifiable as soft matter, which usually present particular nanoscale structures. Fundamental understanding of the dynamical and mechanical properties of soft matter is important for bioscience and biomedical applications.

In order to mimic cell membrane system by polymer ultrathin films, the control of nanostructure is crucial due to the strong influence of morphology to properties and performances. Herein in this thesis, the author focuses on the methodology to construct the polymer ultrathin films with nanostructures and their possibility as a model for biological soft matter systems.

This thesis is consisted of six chapters. Chapter 1 deals with some core principles of soft matter and polymer ultrathin films. The major features of soft matter were discussed foremost. In particular, biosystems, such as cell membrane system were emphasized. Then, the concept of polymer ultrathin films was introduced. The author reviewed the nanofabrication technologies for preparing nanostructures, especially focusing on polymer phase separation based self-assembly technology. In Chapter 2-3, fundamental methodology to construct polymer ultrathin films with nanostructures was established. A simple model for the phase separation mechanism within ultrathin films was proposed, which was expected to play an important role in the formation of desired nanostructure. In Chapter 4-5, based on the development of atomic force microscopy theory, the deformation behavior of nanostrucured polymer ultrathin was investigated. The author established a correlation between surface deformation and tip-sample interaction and first proved the plastic deformation at nanoscale is associated with energy dissipation in a controllable manner. Finally, the conclusions and the future prospects of this thesis are described in Chapter 6.

The author is convinced that nanostructured polymer ultrathin films would become an innovative experimental model for biological soft matter systems in both theoretical research and practical applications.

July, 2012

Hong Zhang

Contents

Chapter 1

Fundamental Aspects of Soft Matter, Polymer Ultrathin Films and other Related Fields

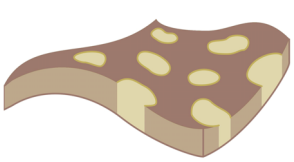

1. Introduction

In this thesis, the author focuses on the methodology to construct the polymer ultrathin films with nanostructures and their possibility as a model for biological soft matter systems.

Chapter 1 mainly deals with some core principles of soft matter and polymer ultrathin films. As the major features of soft matter, complexity and flexibility was discussed foremost. In particular, biosystems, such as cell membrane system were emphasized from a viewpoint of soft matter. Then, the concept and the anomalous behaviors of polymer ultrathin films were introduced. The author reviewed the nanofabrication technologies for construction of polymer based nanostructures, especially focusing on polymer phase separation based self-assembly technology. The basic principles of phase separation behavior of polymer blend or block copolymer were also described in this chapter.

2. Fundamental Aspects of Soft Matter

2-1. Concept of Soft Matter

Soft matter is a material that displays solid-like properties but is distinct form traditional materials in that it is more deformable and liquid-like [1]. The mechanical response of soft matter is often intermediate between solid and liquid. Many such materials are common in everyday life, such as glues, paints, soaps, etc. Much of the food we eat can also be classified as soft matter. We are ourselves soft matter as well as the material we are made of is soft matter [2].

Pierre Gilles de Gennes, who has been called the “founding father of soft matter”, received the Nobel Prize in physics in 1991 for bringing order into soft matter, particularly liquid crystals and polymers [3]. According to his definition, soft matter

can include colloids, gels, surfactants, liquid crystals, polymers, granular materials, and a number of biological materials (Figure 1-1). A characteristic feature of soft matter is the delicate interplay of entropy with various non-covalent interactions, which leads to anomalous behaviors, such as self-assembly and complex phase transition of soft matter systems [2].

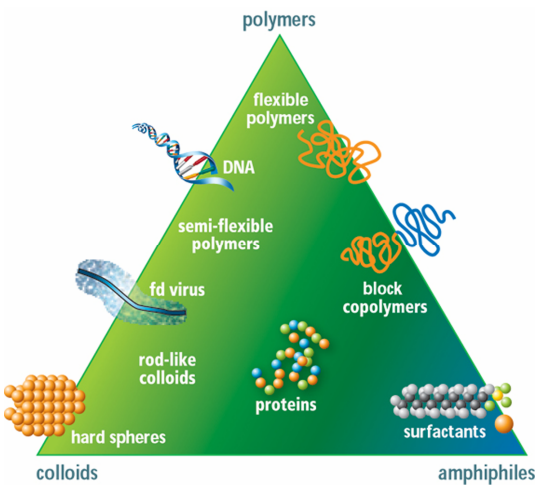

Figure 1-1. Building blocks of soft matter pyramid (depicted from lecture notes of IFF Juelich spring school on Soft Matter, 2008).

2-2. Features of Soft Matter

The fundamental feature of soft matter is its nonlinear response and sensitivity to tiny influence, also called the complexity and flexibility by Pierre Gilles de Gennes [3]. The temperature range relevant for soft matter is roughly between 273 and 500 K, where its behaviors occur at an energy scale comparable with room temperature thermal energy and the interactions between soft matter macromolecules are often entropic in origin. For example, one is able to expand a rubber band to double its size by applying relatively small force, because one is doing work against entropic forces

instead of the forces originating from the chemical bond.

Interesting behaviors arise from soft matter cannot be predicted, or are difficult to predict. This is often because soft matter self-assembly into mesoscopic physical structures that are much larger than the microscopic scale (atomistic and quantum), and yet are much smaller than the macroscopic (overall) scale of the material. The properties and interactions of these mesoscopic structures may determine the behavior of the soft matter (Figure 1-2). The complex structures and dynamics of soft matter are large and slow compared to the atomic scale. Because of its interdisciplinary nature, there is considerable overlap in the field of soft matter physics, physical chemistry and biological science in different aspects, the underlying science, self-assembly, material engineering, as well as the techniques that can be used.

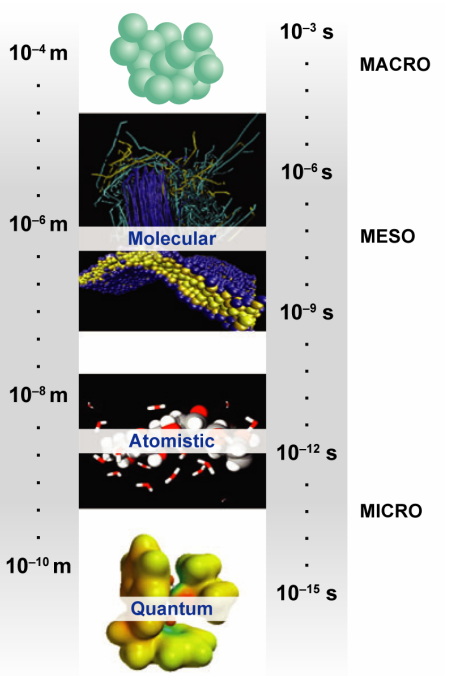

Figure 1-2. Length and time scales of soft matter (depicted from [4]).

3. Fundamental Aspects of Biosystems

3-1. Complexity of Biological Soft Matter System

A biosystem is defined as a system that involves biological macromolecules as the building blocks, which is intrinsically a multi-scale system. For example, genes and proteins are biosystem on the level of molecular biology. Cellular organelles, single cells, organs, and even our human body can also be deemed as biosystem on a specific grade level. At the nanoscale and mesoscale, a number of biosystems are classifiable as soft matter, such as cell membrane, protein composite, etc., which usually present particular nanostructures.

Biological soft matter systems are able to perform a number of vital activities such as protein folding, membrane transport, and cell division, etc [5]. In brief, the precise control of their multi-component and multi-morphology in actual biosystems have dramatically influences on their biological functions, which also always coupled with the change of their viscoelastic property and rheological behavior as typical features of soft matter systems. Obviously, fundamental understanding of the dynamical and mechanical properties of biological soft matter system is important for bioscience and biomedical applications. However, owing to the complexity of biological soft matter systems, current experimental approach still has its limitations.

3-2. Complexity of Cell Membrane System

The cell membrane is a biological membrane that separates the interior of all cells from the outside environment, which basically protects the cell from outside forces. Its structure consists of complex amphiphilic lipid, which has a hydrophilic head with two hydrophobic tails (Figure 1-3). The head is surrounded by water and the cell membrane consists of two layers of lipid suitably arranged, typically ~10 nm. When a

large number of lipid molecules are dispersed in water, the tails will try to avoid the water. The molecules will thereby arrange themselves in a bilayer such that the heads face the water and tails face away from the water and are in contact with other tails. This is the simple principle by which lipid molecules self-assemble and form stable cell membrane, namely the main driving force in the formation of cell membranes is the delicate balance of hydrophilic and hydrophobic properties of head and tail respectively, which also exhibit the feature of soft matter.

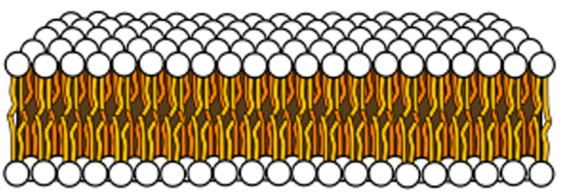

Figure 1-3. Illustration of cell membrane bilayer structure.

As an example of how important multi-component and multi-morphology features of a cell membrane soft matter system influences its vital activities, lipid raft structure is discussed below. Lipid rafts are phase separated domains observed within lipid membranes (Figure 1-4). A definition has been made as “membrane rafts are small (10-200 nm) heterogeneous, dynamic, sterol- and sphingolipid-enriched domains that compartmentalize cellular processes” [6]. Lipid rafts are more ordered and tightly packed compared with the surrounding bilayer, but float freely in the membrane bilayer as well.

Many types of protein are known to interact with lipid rafts, in particular proteins modified by the addition of saturated phospholipid derivatives, which anchor the proteins to the membrane. Many signaling and receptor proteins are modified in this

way, pointing to the importance of lipid rafts in signal transduction. Viruses can also exploit these receptor pathways by binding to signaling proteins in lipid rafts. Lipid rafts may therefore play a role in the transmission of certain infectious diseases.

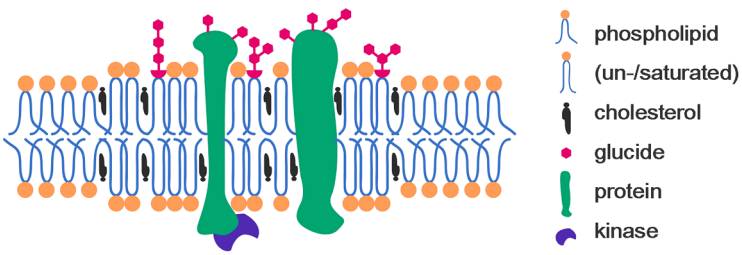

Figure 1-4. Illustration of cell membrane lipid raft structure.

In addition, lipid rafts have been implicated in processes such as endocytosis, exocytosis, and vesicular trafficking (transport of vesicles across the cell). Endocytosis involves the capture of external species by folding the cell membrane around them and budding off of the membrane to form vesicles within the cell. Exocytosis involves the fusion of intracellular fluid-filled vesicles with a cell membrane. In all of these processes, lipid rafts may assist vesicle budding or fusion by contributing to regions of enhanced membrane curvature that result from the lateral phase separation of lipids with different degrees of packing.

From a viewpoint of progress made not only in lipid raft, but also in cell biology in general, questions yet to be answered include: (1) what are the effects of membrane protein levels? (2) what effect does flux of membrane lipids have on raft formation? (3) what is the physiological function of lipid rafts? (4) what effect do diet and drugs have on lipid rafts? (5) what effect do proteins located at raft boundaries have on lipid rafts? [7] In order to solve these problems, it is reasonable to expect an experimental model

for biosystems, such as to mimic the behaviors of cell membrane lipid raft structure, which has multi-component and multi-morphology to exhibit the features of soft matter but relatively easy to be prepared.

4. Principles of Polymer Ultrathin Films

4-1. Concept of Polymer Ultrathin Films

Polymer is macromolecule that composed of repeating structural units. It is known that the properties of a polymer depend not only on the type of its repeating units (monomers), but also on the secondary and tertiary structures, namely the stereochemistry of the linkage, the chain length, entanglement and its distribution, its ability to crystallize or remain amorphous at various conditions, and the shape or distribution of the shapes of the chain in the crystalline and amorphous states [8]. As to polymer films, when the thickness decreases to the dimensions comparable to the dimensions of a single polymer chain, namely polymer chains are confined to nanoscale dimensions, the fundamental characteristics of polymer will significantly changed and induce behaviors that not seen in the bulk [9].

Polymer ultrathin films are also called “thin polymer films” or “nanosheet” in this thesis. Polymer films of whose thicknesses are less than about twice the radius of gyration of an unperturbed chain ($2R_g$) can be defined as ultrathin films [10, 11]. The polymer blend films with thicknesses less than $2R_g$ of the higher molecular weight component can be defined as the ultrathin blend films [12]. The polymer chain in an ultrathin film is in a nonequilibrium state, since the conformational entropy of an individual chain in a constrained region is reduced in comparison with that in bulk state. Therefore, it is reasonable to expect that the molecular aggregation structure in the polymer ultrathin films must be greatly different form that in the thick films [9].

4-2. Polymer Ultrathin Films on Substrate

Several techniques have been developed to construct polymer ultrathin films on substrate. For example, the Langmuir-Blodgett (LB) film, the layer by layer (LbL) film and self-assembled monolayer (SAM) can be constructed on various interfaces such as solid substrate and liquid interface. The polymer ultrathin films were first fabricated by using self-assembly LB technique, in which monolayer is formed on a water surface and subsequently transferred onto a solid support [13, 14] (Figure 1-5). It is the first true nanomanipulations that allows for mechanical handling of individual molecular layer such as separation and contact formation with ultrathin film.

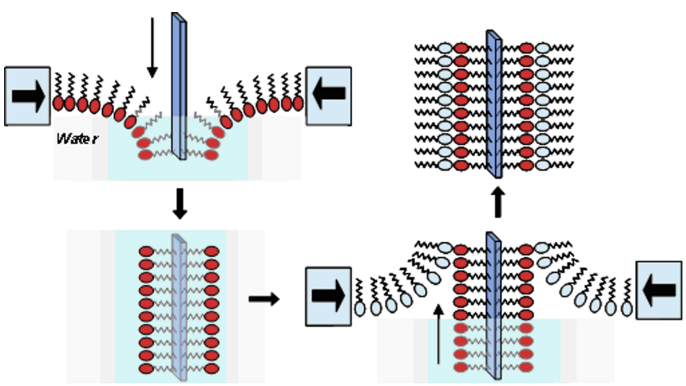

Figure 1-5. Illustration of LB technique for preparing monolayer (depicted from [15]).

Another methodology for the fabrication of nanoscale ultrathin film involving a wide variety of polymers is an LbL technique. The LbL method involves alternative adsorption of oppositely charged polyelectrolytes by different non-covalent linking such as electrostatic interactions, hydrogen bonding or hydrophobic interactions [16] (Figure 1-6). Template assisted assembly is much faster than chemical modification cycles whose outcome is often uncertain or difficult to predict. In the case of LbL technique, it can be tailored to allow multimaterial assembly of several compounds

without special chemical modifications.

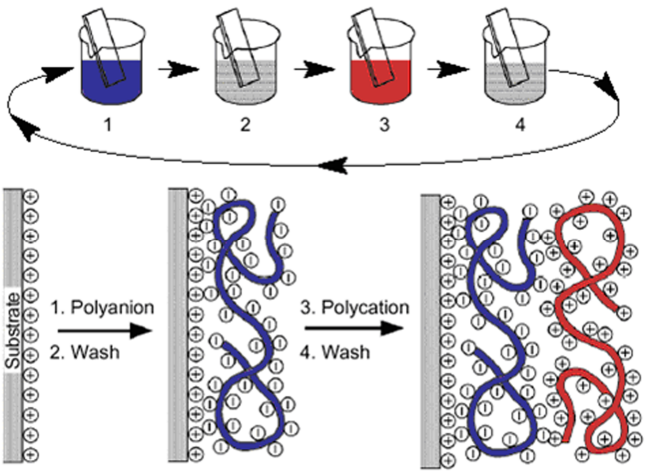

Figure 1-6. Illustration of LbL technique for preparing an ultrathin film (depicted from [17]).

SAM technique was introduced based on constituent molecules, such as thiols and silanes [18, 19]. For SAM, synthetic chemistry is used only to construct the basic building blocks, and weaker intermolecular bonds such as van der Waals bonds are involved in arranging and binding the blocks together into an ultrathin film (Figure 1-7). This weak bonding makes solution, and hence reversible, processing of SAM. Thus, solution processing and manufacturing of SAM offer the enviable goal of mass production with the possibility of error correction at any stage of assembly.

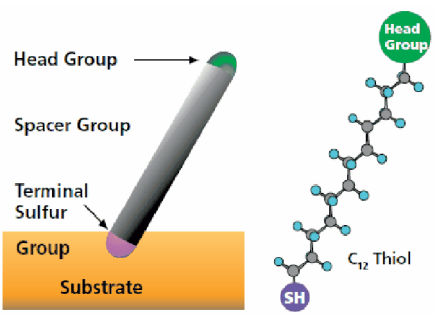

Figure 1-7. Illustration of SAM technique for preparing monolayer (depicted from [20]).

4-3. Features of Polymer Ultrathin Films

There were a large number of studies which have proven that the polymer ultrathin films possess some unique properties of soft matter, such as flexibility, adhesiveness and permeability, which are different from those of bulk polymer films. For example, it has been widely shown that the glass transition temperature (T_g) of thin polymer films differs from that of bulk due to the counterbalance of free surface effect and interfacial effect, i.e., the enhanced mobility of polymer at the free surface coupled with the depressed mobility at the substrate [21-24] (Figure 1-8). Other reports argued against this result and suggested that the change in T_g was a result of residual stress and not due to the intrinsic change of polymer mobility [25, 26].

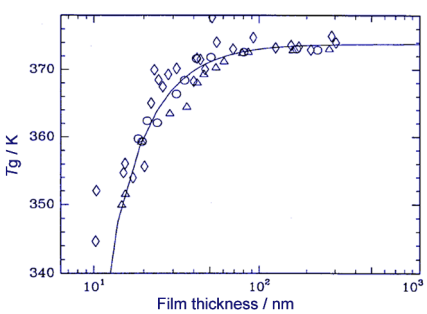

Figure 1-8. Glass transfer temperature versus film thickness of polystyrene films supported on silicon, *Mw* of 120,000 (circles), 500,000 (triangles) and 2,900,000 (diamonds) (depicted from [21]).

Studies of polymer ultrathin films have primarily focused on interpreting the effect of confinement on T_g, while investigations of their other temperature induced properties, such as mechanical properties are still very limited and with a lot of conflicting results. Some reports showed that the apparent elastic modulus of polymer ultrathin films decrease by using a buckling-based metrology [27, 28], also called

strain-induced elastic buckling instability for mechanical measurements (SIEBIMM), which required the film to be transferred onto a relatively soft and thick substrate. It was shown that compared with bulk polymer films, polymer ultrathin films are always rather compliant and exhibit obvious features of soft matter (Figure 1-9).

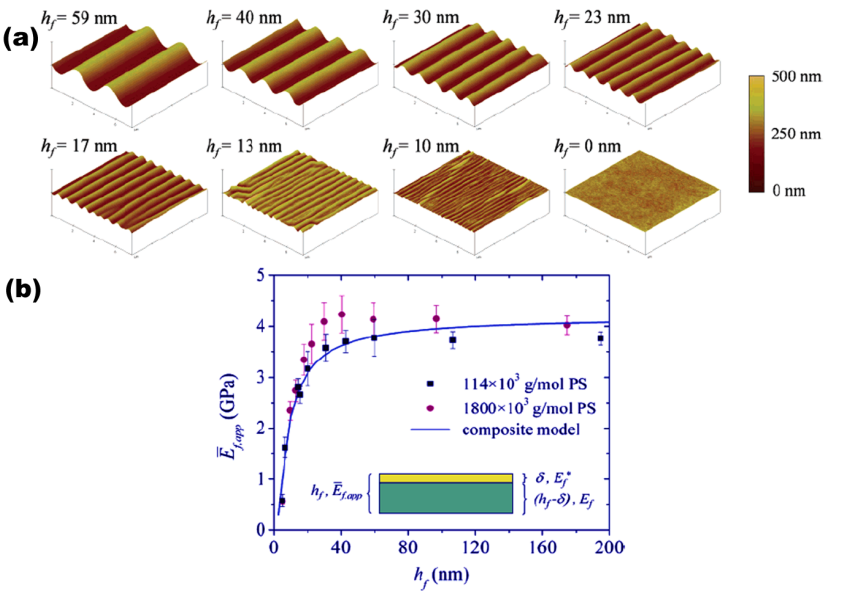

Figure 1-9. Apparent modulus of polystyrene films measured by SIEBIMM method. (a) AFM height images of buckling patterns of polystyrene films (*Mw* of 1,800 kDa) supported on PDMS for various film thicknesses (h_f). (b) Apparent modulus versus film thickness of films (depicted from [28]).

5. Principles of Polymer Based Nanostructures

5-1. Concept of Polymer Based Nanostructures

Systems with at least one structural size below 100 nm are considered nowadays as new classes of materials: the so-called nanostructured polymers or polymer based nanostructures (Figure 1-10). However, nanomaterials of rubber carbon black composites have existed already for nearly one century, and biomedical materials such

as bone, teeth, and skin also have been known for millions of years. Thus, although, the class of nanomaterials is not totally new, rapid development of research activity aiming for a better understanding of the basic mechanisms contributing to the properties of this class of remarkable systems has been recently observed [29].

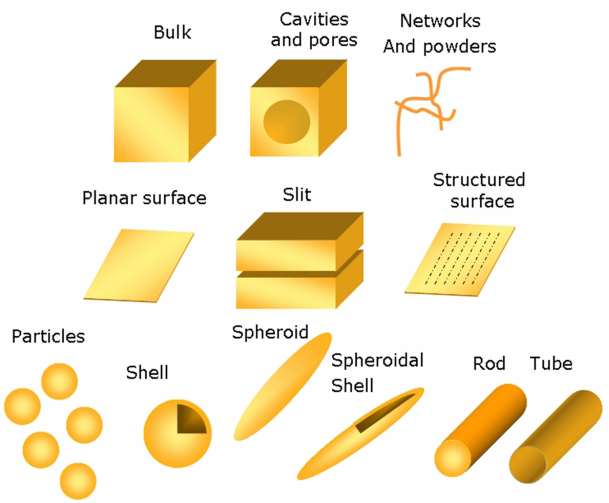

Figure 1-10. Illustration of nanostructure geometries (depicted from The Open source Handbook of Nanoscience and Nanotechnology).

Natural materials, like cell membrane or bone structure, reveal more and more complex hierarchical nanostructures with highly specific functions that have been optimized during evolution over very long periods of time. Far off these biomaterials, in most synthetic polymer blends and composites the hierarchical nanostructure is most formerly created accidentally during synthesis or processing. But now, owing to its importance not only in basic research field but also practical applications, a number of nanofabrication techniques to prepare polymer based nanostructures have been developed and improved over time.

5-2. Strategies of Polymer Based Nanostructures

Nanofabrication is a serious of approaches that would allow preparing nanostructures with atomic precision or the processing of materials with the desired structural, mechanical, optical, magnetic or electronic properties. Generally, the nanofabrication methods are divided into two major categories: “top-down” and “bottom-up” methods according to the processes involved in creating the nanoscale structures. A top-down approach is to create nanostructures with the desired shapes and characteristics starting from larger dimensions and reducing them to the required values. On the other hand, bottom–up approaches seek to have molecular or atomic components built up into nanostructures or directed self-assemblies based on complex mechanisms and technologies [30].

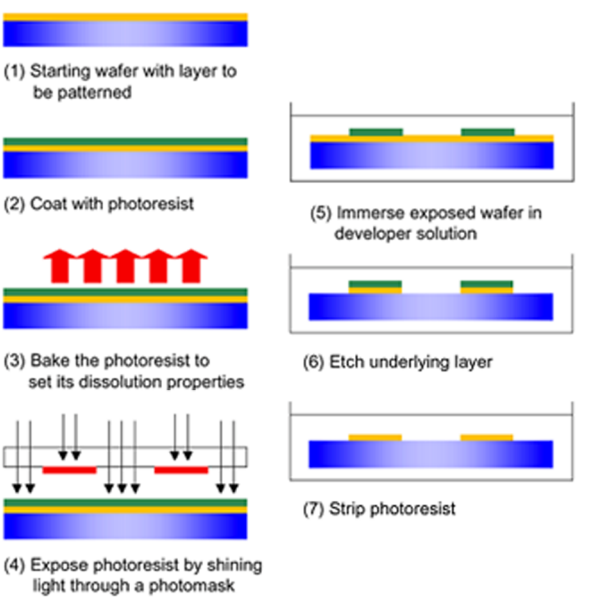

Figure 1-11. Illustration of optical lithography.

Various methods of lithography are used in the top–down approach. In

conventional lithography, required polymer is usually protected by a mask and the exposed material is etched away. Chemical etching using acids or mechanical etching using ultraviolet light, X-rays, or electron beams is performed that determines the feature resolutions of the final product (Figure 1-11). Conventional optical lithography is a simple technique that makes possible a resolution of about 1 μm using light of 400 nm, whereas difficult to achieve a higher resolution [31].

Bottom–up nanofabrication approaches are related to the construction of multifunctional nanostructures by the self-assembly of atoms or molecules. As mentioned above, LbL and SAM techniques are typical examples for bottom-up methods to prepare nanoscale ultrathin film. Bottom-up methods can be classified into three categories: chemical, physical, and colloidal self-assembly. Chemical self-assembly involves molecular level ordering. It is a chemical synthesis process whereby molecules are combined into new structures by non-covalent interactions. Physical self-assembly is the ordering of inorganic atoms during a physical deposition process such as molecular beam epitaxy (MBE) or chemical vapor deposition (CVD). Colloidal self-assembly refers to self-assembly of particles or spheres with diameter from micrometers to nanometers in a liquid suspension (Figure 1-12).

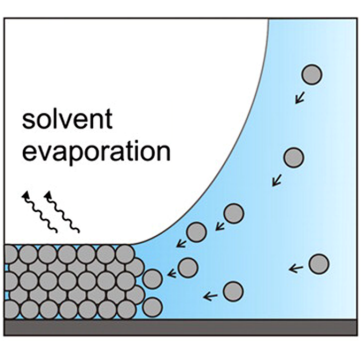

Figure 1-12. Illustration of colloidal self-assembly (depicted from [32]).

5-3. Principles of Polymer Phase Separation

Polymer blends and composites are widely used for preparing nanostructures for their intrinsic immiscibility, as a bottom-up method. The spatial arrangement is controlled by the thermodynamics, whereas the dynamic properties as the phase diagram or the Huggins-Flory binary interaction parameter (χ_{12}) is difficult to determine [8]. A typical phase diagram for polymer blend is shown as Figure 1-13.

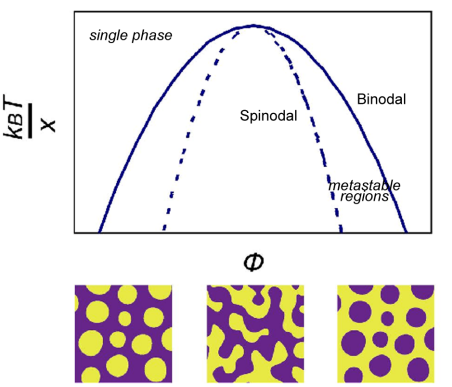

Figure 1-13. The phase diagram for typical polymer blends with upper critical solution temperature.

There are two mechanisms in terms of polymer phase separation: nucleation growth (NG) and spinodal decomposition (SD) [33]. NG mechanism is expected when a system left the thermodynamically stable region and slowly entered the metastable region of the phase diagram. SD mechanism was favored when a system in a rapid quenching entered into the unstable region or even in a slower transition crossed the metastable region near the critical point. There is a drastic difference between them. For NG, there is a large fluctuation in concentration and an energy barrier has to be overcome for the formation of a nucleus isolated droplets of the minor polymer phase in the major phase. However, for SD, there is high interconnectivity between phases in

the early stages of phase separation domains but energy barrier is absent (Figure 1-14).

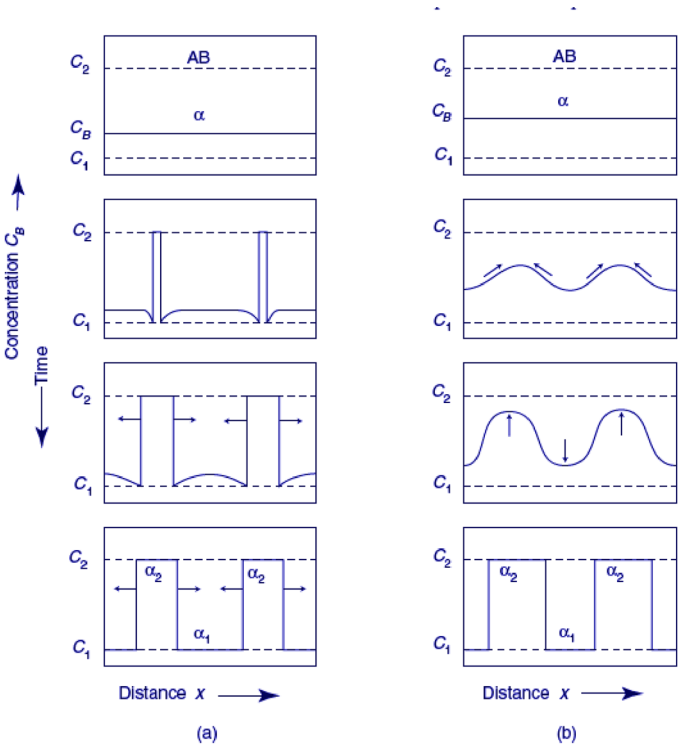

Figure 1-14. Illustration of polymer blend phase separation. (a) NG mechanism and (b) SD mechanism (depicted from [34]).

A special kind of polymer composite is called "block copolymer", which are made up of blocks of different polymerized monomers. The self-assembly of block copolymer into arrays of nanoscale elements makes them ideal candidates for fabrication of polymer based nanostructures. As shown in Figure 1-16, A and B are two blocks monomers of copolymer but immiscible. Similar to polymer blend, A and B would like to segregate, but the full-scale phase separation is impossible because of the presence of a covalent link between them. The result of this conflict is the so-called microphase separation with the formation of A and B rich domains.

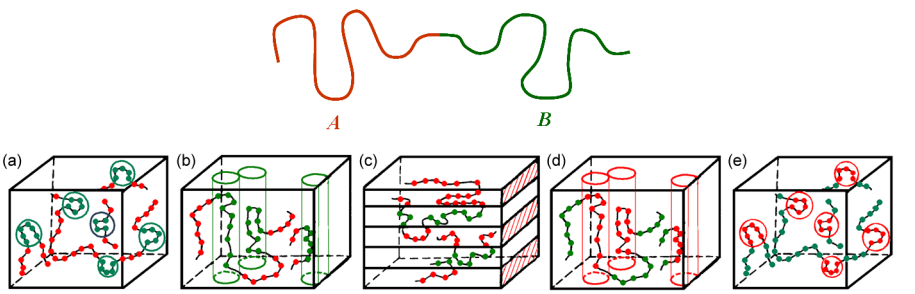

Figure 1-15. Illustration of microphase separation of block copolymer. (a) Spherical B micelles in A surrounding, (b) Cylindrical B micelles in A surrounding, (c) Alternating A and B lamellae, (d) Cylindrical A micelles in B surrounding, and (e) Spherical A micelles in B surrounding.

The preparation of polymer ultrathin films under various solvent evaporation conditions is an effective way to manipulate the orientation and lateral ordering of nanostructures in thin films. The solvent evaporation rate is one of the key factors that control these kinetically trapped nanostructures. For example, inverted phases consisting of spheres or cylinders of the majority fraction block in a block copolymer film, which were not predicted on the basis of typical thermodynamic considerations for block copolymer as shown above, were observed by the control over the solvent evaporation conditions (Figure 1-16). The process is independent of substrate, but strongly dependent on the solubility of the solvents for each block and the solvent evaporation rate.

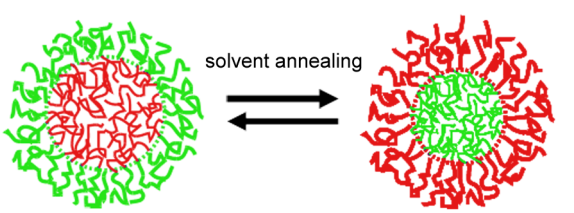

Figure 1-16. Illustration of block copolymers micellization in selective solvents.

References

1. P.G. de Gennes, *Soft Matter*, 2005, 1, 16.

2. R.A.L. Jones, *Soft Condensed Matter*, Oxford University Press, 2002.

3. P.G. de Gennes, *Nobel Lecture*, 1991.

4. M. Praprotnik *et al*., *Annu. Rev. Phys. Chem.*, 2008, 59, 545.

5. I.W. Hamley *et al*., *Angew. Chem. Int. Ed.*, 2007, 46, 4442.

6. L.J. Pike, *J. Lipid Res.*, 2006, 47, 1597.

7. L.J. Pike, *J. Lipid Res.*, 2009, 50, S323.

8. J.E. Mark. *Physical Properties of Polymers Handbook*, Springer Science, 2007.

9. O.K.C. Tsui *et al*., *Polymer Thin Films*, World Scientific Publishing, 2008.

10. K. Shuto *et al.*, *Macromolecules*, 1993, 26, 6589.

11. K. Tanaka *et al*., *Macromolecules*, 1996, 29, 3232.

12. K. Tanaka *et al*., *Macromolecules*, 1995, 28, 934.

13. K.B. Blodgett, *JACS*, 1934, 56, 495.

14. H. Kuhn *et al*., *Angew. Chem. Int. Ed.*, 1971, 10, 620.

15. C.P. Michael, *Langmuir-Blodgett Films*, Cambridge University Press, 1996.

16. G. Decher *et al*., *Thin Solid Films*, 1992, 210, 831.

17. G. Decher *et al*, *Multilayer Thin Films*, Wiley-VCH, 2003.

18. R.G. Nuzzo *et al*., *JACS*, 1983, 105, 4481.

19. M.R. Linford *et al*., *JACS*, 1993, 115, 12631.

20. B. Maxi *et al*., *Material Matters*, 2006, 12, 3.

21. J.L. Keddie *et al*., *Europhys. Lett.*, 1994, 27, 59.

22. J.A. Forrest *et al*, *Phys. Rev. Let*t., 1996, 77, 2002.

23. D.S. Fryer *et al*., *Macromolecules*, 2000, 33, 6439.

24. C.B. Roth *et al*., *Macromolecules*, 2007, 40, 2568.

25. H.Y. Lu *et al*., *Macromolecules*, 2009, 42, 9111.

26. M. Tress *et al*., *Macromolecules*, 2010, 43, 9937.

27. C.M. Stafford *et al*., *Nat. Mater.*, 2004, 3, 545.

28. C.M. Stafford *et al*., *Macromolecules*, 2006, 39, 5095.

29. G.H. Michler *et al*., *Mechanical Properties of Polymers based on Nanostructure and Morphology*, Taylor & Francis Group, 2005.

30. A. Biswas *et al*., *Adv. Colloid Interface Sci.*, 2012, 170, 2.

31. B.D. Gates *et al*., *Chem. Rev.*, 2005, 105, 1171.

32. B. Hatton *et al*., *PNAS*, 2010, 107, 10354.

33. P.G. de Gennes, *Scaling Concepts in Polymer Physics*, Cornell University Press, 1979.

34. L.A. Utracki, *Polymer Blends Handbook*, Kluwer Academic Publishers, 2002.

Chapter 2

Construction of Nanostructured Polymer Ultrathin Films and their Formation Mechanism

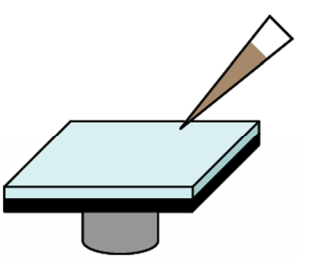

1. Introduction

Polymer phase separation has established a series of bottom-up nanofabrication methods. Owing to the intrinsic immiscibility of most polymer blends, phase separation is typically produced by rapid quenching during spin-casting. However, the full sequence of events that occur during this process is still unclear, especially in the case of polymer ultrathin films.

In this chapter, the author established the polymer blend phase separation assisted construction method to prepare ultrathin films with nanostructures and proposed a mechanism of their formation. The evolution of the morphological structure within spin-casting polymer blend ultrathin films was investigated by a solvent etching technique in combination with a freestanding method for the first time.

2. Construction of Polymer Ultrathin Films with Nanostructures

2-1. Routines for Film Preparing

The polymers used in this study were polystyrene (PS) (Mw = 170,000; Mw/Mn = 1.06; d = 1.05 g/cm^3) and poly(methyl methacrylate) (PMMA) (Mw = 120,000; Mw/Mn = 1.8-2.0; d = 1.19 g/cm^3), which were purchased form Chemco Scientific Co., Ltd. (Osaka, Japan) and Sigma-Aldrich (St Louis, MO), respectively. Water-soluble poly(vinyl alcohol) (PVA) (Mw = ~22,000) used for preparing a sacrificial layer was purchased form Kanto Chemicals Co., Inc. (Tokyo, Japan). All chemicals were used without further purification.

The spin-casting substrates used in this study were silicon (100) wafers covered with 200 nm thermally grown silicon oxide (SiOx) purchased from KST World Co., which were cut into a size of 20 × 20 mm^2. Substrates were cleaned at 120 °C in a piranha solution of sulfuric acid and 30 % hydrogen peroxide (3:1, v/v) for 15 min and

then thoroughly rinsed with deionized water (18 MΩ cm) and dried with compressed nitrogen gas. The static water contact angle of a clean silicon substrate was measured to be approximately 44.5° with a commercial contact angle meter (DM-301, Kyowa Interface Science Co., Ltd.).

Polymer blend solutions were prepared by dissolving PS and PMMA with various weight ratios (PS:PMMA = 0:10, 1:9, 2:8 and 3:7 w/w) in analytic grade CH_2Cl_2 as common solvent, and were proposed to stand overnight before film preparation in order to achieve complete dissolution. The total polymer concentration in the solutions was 1.0 wt% unless otherwise noted. The ultrathin polymer blend films were prepared by a spin-casting method using a spin coater MS-A100 (MIKASA Co., Ltd.) as follows. First, PVA as a sacrificial layer was prepared by spin-casting at 3000 rpm for 60 s from a PVA aqueous solution (1.0 wt%) onto a clean substrate. Then polymer blend solution was dropped onto this PVA-coated substrate and spin-casted at various rotating speeds (1000, 3000, 5000 and 7000 rpm) for 60 s. Finally, the as-cast blend films were immersed into deionized water. By the dissolution of the underlying PVA sacrificial layer, the resulting film could be detached from the silicon substrate and sustain their shape on the water surface [1, 2]. Furthermore, during the freestanding process the bottom side of the film could be obtained by a careful operation to reverse the thin film from its edges with a tweezers. It was worth noting that the bottom side of the 3:7 w/w blend ratio film was actually obtained by overlapping the film with bottom side upward, since the strength of the ultrathin films prepared with 3:7 w/w blend ratio were too low to be reversed completely during the freestanding process.

Cyclohexane is a good solvent for PS and poor solvent for PMMA [3]. In most cases of this study, before freestanding, the as-cast blend films were immersed into cyclohexane overnight to give sufficient contact time for selective removal of the PS

regions and washed with copious amounts of the cyclohexane afterwards. The freestanding films (top or bottom side) were re-supported on the surface of another clean silicon substrate for subsequent morphological characterization. All routines for film preparation were conducted at room temperature (25 °C) and normal relative humidity (35% RH) in a clean room (class 10,000 conditions) to avoid contamination. The schematic illustration of construction of polymer thin films with nanostructures can be found in Figure 2-1.

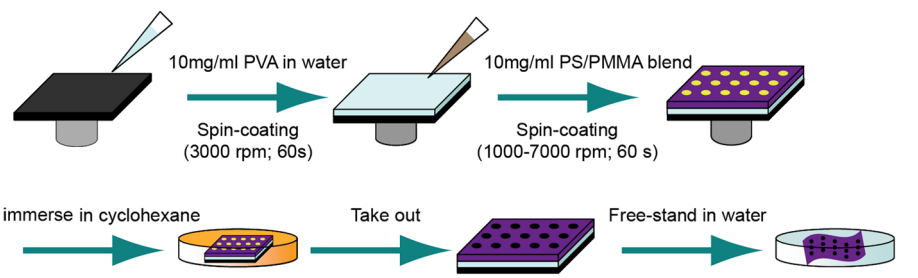

Figure 2-1. Illustration of construction of polymer thin films with nanostructures.

2-2. Characterization Tools for Ultrathin Films

To investigate the topography of the prepared films, atomic force microscopy (AFM) was performed with a KEYENCE VN-8000 NANOSCALE hybrid microscope. The images were collected in a tapping mode with a silicon cantilever (KEYENCE, OP-75041) at a scan rate of 1.67 - 3.33 Hz under ambient conditions. The thickness of the thin films was determined by scratching the samples with a scalpel and then measuring the lateral profile with AFM. The AFM images were analyzed using VN Analyzer (KEYENCE) and ImageJ (NIH) software. The shape, size and distribution of phase separation domains exhibited on the resulting films were measured quantitatively.

Field emission scanning electron microscopy (FE-SEM, Hitachi S-5500) was utilized for the observation of the morphology especially the cross sectional view of the prepared films. The films were submerged in liquid nitrogen for 10 min to harden the polymer and then snapped suddenly with tweezers in the liquid nitrogen container. The cross section sample was sputter-coated with gold-palladium (Au-Pd) prior to FE-SEM observation with an accelerating voltage of 5 kV. The brightness and contrast of each SEM image was adjusted for optimal viewing using ImageJ software.

3. Features of Construction Method for Ultrathin Films

3-1. Freestanding of Ultrathin Films

Upon spin-casting, the ultrathin film was immersed into water and then the film spontaneously and gradually detached from the edges of the substrate. It was found that the resulting freestanding ultrathin film floating on the water surface was fully obtained without any shape or size distortion (Figure 2-2 (a)). It was noted that except the PMMA homopolymer ultrathin film (0:10 w/w) with high transparency, the top/bottom side of all the blend films appeared opaque in visual observation, which implied the phase separation had taken place during spin-casting.

The thickness of PVA sacrificial layer was estimated to be 17.2 ± 0.85 nm and revealed this layer was as smooth and flat (RMS roughness 0.81 ± 0.14 nm) as the silicon wafer (RMS roughness 0.75 ± 0.12 nm), without any corrugations and wrinkles. However, the microscopy images of upper ultrathin blend films always exhibited radiative striation flaw in most cases (Figure 2-2 (b)). This topographical defect has been proved a result of unfavorable capillary forces that develop due to the surface tension change, also called Marangoni instability during solvent evaporation in a spin-casting process [4]. In this study, the author found that the tiny thickness

undulations induced by striation flaw had very limited influence on phase separation morphology of an ultrathin film; thus this effect was not studied systematically further.

Our previous studies have demonstrated that the freestanding method is an efficient means of transferring the ultrathin film from a solid substrate to various other surfaces, such as human skin [5] and animal organs, as shown in Figure 2-2 (c) [6-8]. Herein, by using this procedure, the bottom side of the film could be observed as well, which allowed us to firstly obtain morphological information from the bottom side of the film.

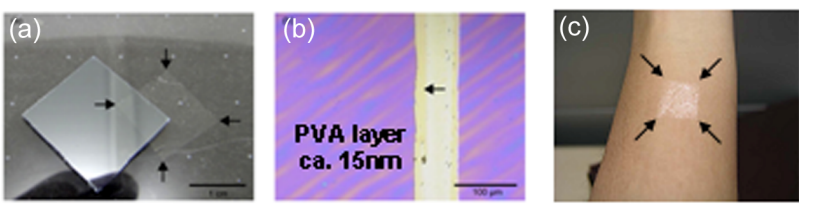

Figure 2-2. Feasibility of freestanding method. (a) photograph of a freestanding ultrathin film; (b) microscopy image of a film with a scalpel scar; (c) transfer the thin film to human skin.

3-2. Discussion of Substrate Surface Energy

A number of studies have shown that the phase separation behavior and morphology features of spin-casting blend films were greatly influenced by the surface energy of substrates [3]. In contrast to bulk systems, the interface interactions must be taken into account when polymer blends restricted to an ultrathin film. In this study, the PVA-coated substrate was first introduced into the phase separation study of spin-casting films. Therefore, the effect of PVA sacrificial layer on phase separation morphology should be investigated foremost. Ultrathin films were spin-casted on PVA-coated substrates or common silicon substrates and all other relevant conditions remained the same. By means of AFM observation, films prepared from these two

types of substrates were found no significant morphology differences within the range of all the preparation conditions in this study (Figure 2-3).

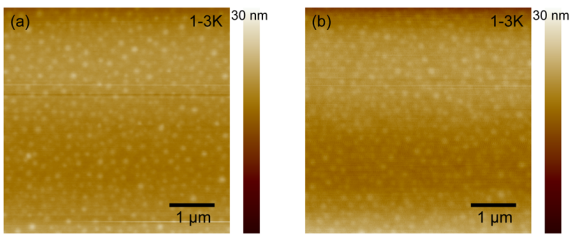

Figure 2-3. AFM height images of films prepared with 1:9 w/w, 3000 rpm; as-cast onto (a) PVA-coated substrate and (b) SiO*x* substrate.

This observation could be interpreted as a consequence of the very close surface energy values of PVA and SiO*x* substrates. Surface energy was obtained by contact angle measurement and calculated using Owens - Wendt's equation: [9]

$$\gamma_{L1}(1+cos\,\theta_1) = 2(\gamma_s^d \gamma_{L1}^p)^{1/2} + 2(\gamma_s^p \gamma_{L1}^p)^{1/2}$$

$$\gamma_{L2}(1+cos\,\theta_2) = 2(\gamma_s^d \gamma_{L2}^p)^{1/2} + 2(\gamma_s^p \gamma_{L2}^p)^{1/2} \quad (2\text{-}1)$$

where γ^d was dispersion component and γ^p was polar component of surface energy. Subscript s, L1 and L2 stood for substrate, test liquid 1 and test liquid 2, respectively. Water and n-hexadecane were chosen as test liquids in this study. The surface energy of test liquids and contact angle results of SiO*x* substrates were listed in Table 2-1.

Using equation (2-1) and contact angle results, the dispersion component γ_s^d and the polar component γ_s^p of cleaned silicon substrate was found to be 27.2 mJ/m^2 and 28.3 mJ/m^2, respectively. Thus the total surface energy would be approximately 55.5 mJ/m^2. Furthermore, the surface energy of PVA obtained by the same method was shown to be

58.7 mJ/m^2 (γ_s^d ~ 33.0 mJ/m^2 and γ_s^p ~ 25.7 mJ/m^2), derived from the previous report [10]. The very close surface energy values of PVA and SiO*x* substrates were probably a result of the chemical structures, i.e., the hydroxyl groups of PVA and silanol groups of SiO*x* at the air-surface. These preliminary experiments proved that the use of PVA sacrificial layer on silicon wafers had no significant effect on phase separation morphology and confirmed that the results obtained in this study would be comparable to the previous studies on spin-casting polymer blend films.

Table 2-1. Surface energy of test liquids and contact angle results. [a]

Test liquid	γ^d (mJ/m^2)	γ^p (mJ/m^2)	Contact angle (deg.)
water	21.8	51.0	44.5
n-hexadecane	27.6	0	9.2

[a] Contact angle measured nine times and shown as average value.

3-3. Discussion of Selective Solvent Etching

The technique of solvent etching was also applied in order to evaluate the distribution of the two polymers, PS and PMMA. By immersing an as-cast blend film into cyclohexane overnight, PS regions were removed. Figure 2-4 (a) and (b) represented typical *in situ* AFM images taken before and after solvent etching, and Figure 2-4 (c) was their 3D image. It was obvious to see that the protrusion domains corresponded to PS regions. The structure as shown in Figure 2-4 (a) obtained from numerous PS droplets embedded in matrix of PMMA. Furthermore, as to the shape and size of PS regions, namely PS droplets in Figure 2-4 (a) and nanopores in Figure 2-4 (b), there found no differences before and after solvent etching, indicating cyclohexane only dissolved PS regions and proved a good method to observe phase

separation morphology. Figure 2-4 (d) profile was drawn at the same place of Figure 2-4 (a) and (b) to show the PS and PMMA distribution. Note that the different length scale of *x*-axes and *y*-axes in Figure 2-4 (d) was applied. The real shape of PS region was proved to be a flattened droplet.

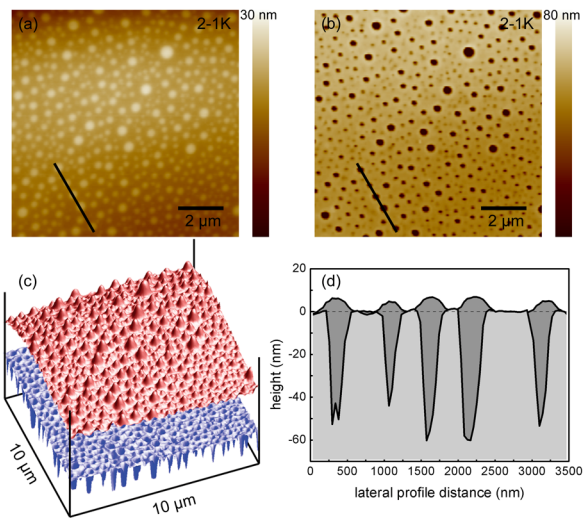

Figure 2-4. *In situ* AFM height images of a film prepared with 2:8 w/w, 1000 rpm; (a) as-cast and (b) top side after solvent etching; (c) AFM 3D images proceed from (a), (b) and displayed together; (d) lateral profile drawn at the line places shown in (a), (b) and displayed together (PS: dark gray; PMMA: light gray).

4. Morphology of Polymer Ultrathin Films with Nanostructures

4-1. Topographical Features of Ultrathin Films

The phase separation within the ultrathin film was the origin of surface topography. The primary aim of this work was to understand how certain preparation conditions influenced the morphological structure after spin-casting. The dependence

of surface topography on polymer blend composition and rotating speed would be discussed below.

AFM images of four typical samples prepared with various polymer blend compositions (0:10, 1:9, 2:8 and 3:7 w/w) and the same rotating speed (5000 rpm) were shown in Figure 2-5. Figure 2-5 (a1) – (d1) presented the surface topography of as-cast blend films. After solvent etching, Figure 2-5 (a2) – (d2) were taken to reveal the surface topography of the remaining PMMA regions on the top side of films. Subsequently, the bottom side of the films were obtained by the freestanding method and observed by AFM again as Figure 2-5 (a3) – (d3). The PMMA homopolymer ultrathin film (PS:PMMA = 0:10 w/w) was flat and fairly featureless (Figure 2-5 (a1)) as expected, whereas the PS/PMMA blend films showed apparent phase separation structures. In the case of the ultrathin films prepared with 1:9 and 2:8 w/w blend ratios (Figure 2-5 (b1) and (c1)), the sea-island like morphology (dispersed morphology) was observed. In the case of the 3:7 w/w blend ratio (Figure 2-5 (d1)), the ribbon like structure (bicontinuous morphology) formed. The bottom side AFM image of the 3:7 blend ratio (Figure 2-5 (d3)) was obtained by measuring an overlapped film with bottom side upward, as mentioned before. Thus, the ribbon like structure of the underlying film could also be seen from the interstitial ribbon space of the upper film, as the arrow shown in Figure 2-5 (d3).

AFM images of four typical samples prepared at various rotating speeds (1000, 3000, 5000, and 7000 rpm) and with the same polymer blend composition (PS:PMMA = 2:8 w/w) are shown in Figure 2-6. The arrangement of Figure 2-6 is similar to that of Figure 2-5. All of the ultrathin films gave an island-like morphology, regardless of the rotating speed used in their preparation. As the rotating speed increased, the size of the

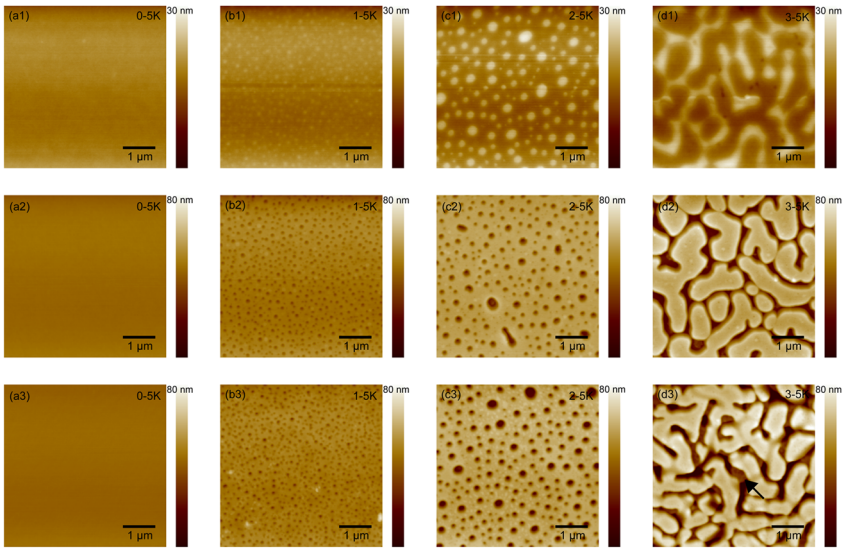

Figure 2-5. AFM height images of films prepared at a rotating speed of 5000 rpm; as-cast (first row), top side (second row) and bottom side (third row) after solvent etching with 0:10 (first column), 1:9 (second column), 2:8 (third column) and 3:7 (fourth column) blend ratios.

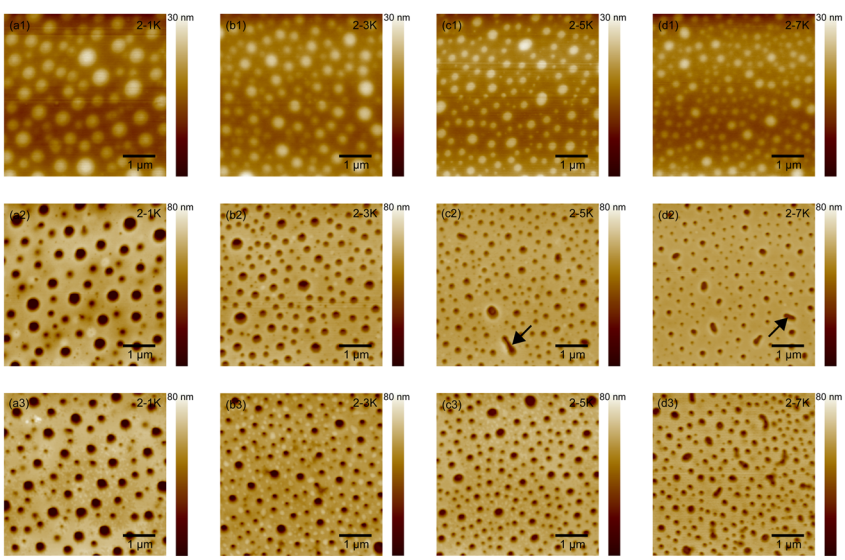

Figure 2-6. AFM height images of films prepared with 2:8 w/w; as-cast (first row), top side (second row) and bottom side (third row) after solvent etching for 1000 rpm (first column), 3000 rpm (second column), 5000 rpm (third column) and 7000 rpm (forth column).

PS regions become smaller, while the total number of PS regions in the area of the AFM image (5 × 5 μm^2) was increased. Furthermore, ultrathin films prepared at high rotating speeds, such as 5000 and 7000 rpm, displayed some irregular structures (arrow shown in Figures 2-6 (c2) and (d2)). The author reasoned that these observations provide an important clue in terms of the phase separation mechanism within the ultrathin films.

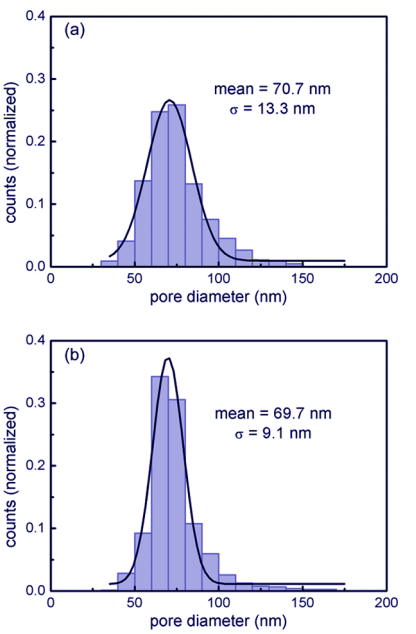

Figure 2-7. Gaussian fitting for the pore diameter histogram of AFM height images of films prepared with 1:9 w/w, 5000 rpm; (a) top and (b) bottom side after solvent etching.

In order to get a deep insight into such topographical features of prepared films, AFM images were quantitatively examined. Here, for a variety of preparation conditions, the thickness of the prepared ultrathin film was measured first, as listed in Table 2-2. The results indicated that the thickness could be adjusted in the range from

~40 to ~110 nm by varying the preparation conditions in this study, which accorded with the concept of an "ultrathin polymer film". After removing PS regions, the size (diameter and area) of the nanopores exhibited on the top and bottom side of resulting films were measured and analyzed by means of statistical methods. For example, Figure 2-7 showed the Gaussian fitting for the pore diameter histogram of the corresponding AFM images Figure 2-5 (b2) and (b3), thus gave mean values of pore diameter. All of the AFM images were analyzed using this method and the results were listed in Table 2-2 as well.

Table 2-2. Film thickness and quantitative measures of phase separation morphology. [a,b,c]

Sample	Thickness	Pore diameter (nm)	Pore area (nm^2)	PS surf. (%)
1-1K	97.6 ± 1.3	102.1 ± 24.4 / 102.3 ± 26.4	9387.7 ± 4096.6 / 9002.7 ± 3619.6	13.8 / 10.8
1-3K	56.7 ± 1.9	81.3 ± 18.6 / 73.1 ± 12.3	6156.5 ± 2851.4 / 5807.1 ± 1910.6	13.6 / 15.5
1-5K	42.6 ± 0.7	70.7 ± 13.3 / 69.7 ± 9.1	4537.8 ± 2314.5 / 4623.6 ± 1651.3	13.5 / 15.6
1-7K	38.8 ± 1.1	64.4 ± 9.3 / 67.6 ± 9.6	3796.4 ± 1251.3 / 4469.8 ± 1611.5	11.1 / 12.3
2-1K	110.2 ± 2.0	187.2 ± 33.9 / 194.1 ± 72.9	27725.8 ± 8794.5 / 21112.5 ± 5774.3	15.5 / 12.4
2-3K	60.6 ± 2.9	148.2 ± 38.7 / 124.5 ± 30.2	16492.0 ± 9753.5 / 13748.3 ± 5854.0	14.4 / 12.9
2-5K	44.4 ± 1.0	116.0 ± 35.5 / 114.5 ± 24.5	12039.3 ± 6404.4 / 13002.7 ± 4333.5	13.6 / 12.5
2-7K	40.4 ± 1.3	105.4 ± 25.1 / 108.2 ± 20.9	10158.8 ± 4143.7 / 10728.3 ± 4040.5	12.0 / 15.4

[a] Thickness values measured five times and shown as mean ± sd.; pore diameter and pore area values derived from Gaussian fitting N (μ, σ^2) and show as $\mu \pm \sigma$. [b] Pore diameter, pore area, and PS surface coverage were shown as top/bottom side values. [c] The samples prepared with 3:7 w/w blend ratio gave bicontinuous morphology; therefore, the morphological information was not listed here.

These findings indicate that altering the preparation conditions changed the thickness of the film and the size of the resulting nanopores in a controllable manner.

For example, in the case of the 2:8 blend ratio, when the rotating speed was increased from 1000 to 7000 rpm, the film thickness was decreased from 110.2 ± 2.0 to 40.4 ± 1.3 nm and the diameter of nanopores was decreased from 187.2 ± 33.9 / 194.1 ± 72.9 to 105.4 ± 25.1 / 108.2 ± 20.9 nm (top/bottom side). The size of nanopores was strongly dependent on the amount of PS component in the blend. For instance, if we consider the results where the blend ratio was increased from 1:9 to 2:8 at a rotating speed of 5000 rpm, the film thickness was slightly increased from 42.6 ± 0.7 to 44.4 ± 1.0 nm with some viscosity changes in the polymer blend solution, but the diameter of nanopores was dramatically increased from 70.7 ± 13.3 / 69.7 ± 9.1 to 116.0 ± 35.5 / 114.5 ± 24.5 nm (top/bottom side).

By analogy with traditional methods, it was found that the shape, size and distribution of nanopores exhibited on both sides of ultrathin films were essentially consistent with each other. For example, statistical analysis of the differences in pore area on both sides were compared using the *t* test (paired, 2-tailed), which confirmed that there was no significant difference ($p = 0.32 > 0.05$). This unexpected result raised the possibility that the resulting nanopores might penetrate the entire thickness of the film. Thus, the author devised a rough method to confirm whether the film was perforated based on PS surface coverage, which was obtained by taking the sum of the area occupied by PS regions divided by the total area of the AFM image. These data are also listed in Table 2-2.

Figure 2-8. Illustration of cross section of an as-cast ultrathin polymer blend film (PS: dark gray; PMMA: light gray).

A schematic picture was drawn as shown in Figure 2-8, where the PS droplet was considered to be rectangular in cross section for simplicity. Two morphological parameters *h'* and *h*, were defined as the height of the PS domains and the height of PMMA domains, namely the thickness of ultrathin film. The total area of the ultrathin film was denoted by *S*. Therefore, the volume of PS component V_{PS} and PMMA component V_{PMMA} could be written as

$$\alpha Sh' = V_{PS} \quad \text{and} \quad (1-\alpha)\, Sh = V_{PMMA} \qquad (2\text{-}2)$$

where α was PS surface coverage. From Equation (S2), the height ratio of PS domains to PMMA domains *k* could be obtained as

$$k = \frac{h'}{h} = \frac{(1-\alpha)V_{PS}}{\alpha V_{PMMA}} = \frac{(1-\alpha)m_{PS}d_{PMMA}}{\alpha m_{PMMA}d_{PS}} \qquad (2\text{-}3)$$

where *m* and *d* denoted mass/weight and density, respectively.

The value of *k* would be a key parameter to reflect phase separation structure and estimate whether the film was perforated or not. In the case of $k < 1$ ($h' < h$), the PS droplets could not penetrate the ultrathin films completely and lead to a film lacking perforations. In the case of $k > 1$ ($h' > h$), the PS droplets were possible to penetrate the ultrathin films and achieve a perforated film. In this study, it was proposed that the weight ratio of PS to PMMA within the ultrathin film was essentially equal to the initial polymer blend solutions. Based on this assumption, in the case of 1:9 w/w blend ratio, the average value of PS surface coverage was taken as 13.3 %, which gave a *k* value of 0.82. In the case of 2:8 w/w blend ratio, the average value of PS surface coverage was taken as 13.6 %, which gave a *k* vale of 1.80.

By applying this procedure, the ultrathin films prepared with a blend ratio of 1:9 cannot be perforated. However, a blend ratio of 2:8 gave nanopores that appear to

penetrate the ultrathin film. These predictions were subsequently verified by the following SEM observations.

4-2. Cross-sectional Views of Ultrathin Films.

Detailed observations of depth profile from AFM are unsatisfactory because the size and shape of the AFM tip is limited. Herein, SEM was applied as a general approach to investigate cross-sectional views of the ultrathin polymer blend films.

SEM images showed that the nanopores were essentially the same as the features derived from the corresponding AFM observations. The cross-sectional SEM images of a film prepared from a 1:9 blend ratio and various rotating speeds (Figure 2-9 (a) and (b)) indicated that the nanopores cannot penetrate the ultrathin film, regardless of the film thickness. This result suggests the film was semi-perforated, in agreement with our predictions based on the AFM data. The results for the 2:8 blend ratio are complicated. Two of the displayed nanopores prepared from a rotating speed of 1000 rpm were deemed to only partially penetrate the ultrathin film, i.e. one was exposed to the top side, while the other was exposed to the bottom side of the film (Figure 2-9 (c)). However, the displayed nanopore within a relatively thinner film prepared from 5000 rpm appeared to completely penetrate the ultrathin film and thereby constitute a perforation (Figure 2-9 (d)). Taken together, our results imply the proportion of nanopores that penetrate the film can be increased by decreasing the film thickness at a given blend ratio.

Figure 2-9 (e1) and (e2) show SEM images of a film surface, which reveal details of the nanopores. This film was prepared with a blend ratio of 2:8 and at a rotating speed of 3000 rpm. The images clearly demonstrate that the nanopores with two quasi-circular boundary lines on both sides of the film penetrate the ultrathin film

(boundary lines highlighted in the figures). In some cases the boundary on the top side was larger than that of the bottom side (arrow shown in Figure 2-9 (e1)). This nanopore forms a lower concave shape indicating the initial PS droplet developed from the top side of the film. By contrast, some nanopores possessed a boundary on the top side of the film that was smaller than that on the bottom side (arrow shown in Figure 2-9 (e2)). In this instance, the shape of the nanopore is upper convex suggesting the PS droplet grew from the bottom side of the film. Therefore, the author concludes that the PS droplets are randomly distributed within the ultrathin films at early stage, which leads to the random distribution of nanopores after solvent etching. Indeed, this

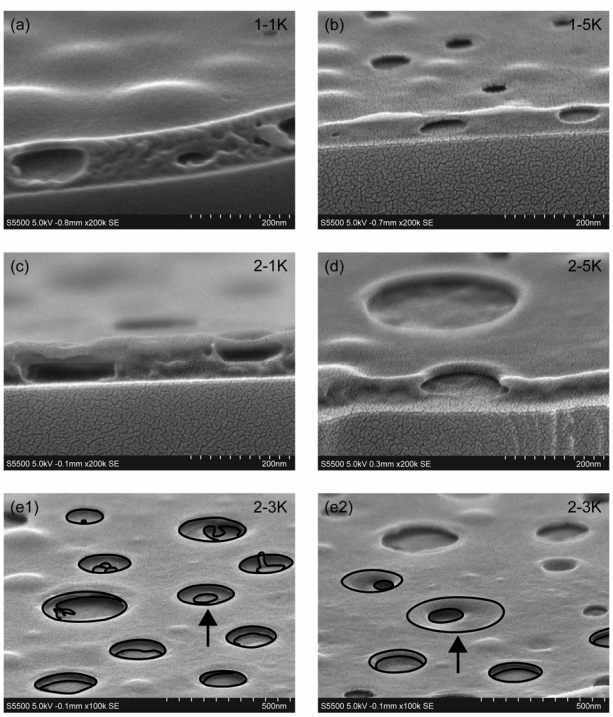

Figure 2-9. SEM images of ultrathin films; cross sectional SEM for (a) 1:9 w/w, 1000 rpm; (b) 1:9 w/w, 5000 rpm; (c) 2:8 w/w, 1000 rpm; (d) 2:8 w/w, 5000 rpm and surface SEM for (e) 2:8 w/w 3000 rpm.

could also explain the location of the nanopores displayed in Figure 2-9 (c).

4-3. Correlation Analyses of Phase Separation Morphology.

In spin-casting, solid films are prepared from a dissolved or dispersed substance by removing the solvent with high-speed spinning. By spin-casting, uniform large areas films could be prepared quickly. The thickness of most films obeys the power law: [11, 12]

$$h \propto \omega^{-2/3}\eta^{1/3}e^{1/3} \ (e \propto \omega^{1/2}) \quad (2\text{-}4)$$

where ω denotes the rotating speed; η denotes viscosity and e denotes evaporation rate of the solvent. Herein, a correlation between the film thickness and the pore size was investigated. As shown in Figure 2-10 (a), the film thickness h was plotted as a function of the rotating speed ω (ω (rad/s) = $2\pi f$ (rpm)). Accorded with the power law,[28,29] films prepared with blend ratios of 1:9 and 2:8 were found to have a thickness h proportional to $\omega^{-0.49}$ and $\omega^{-0.53}$, respectively. Because there was no significant difference between the topographical features on the top and bottom sides, the average value of the pore areas was calculated (referred to as the mean pore area A_{pore}). These values were also plotted as a function of the rotating speed, as shown in Figure 2-10 (b). Films prepared with blend ratios of 1:9 and 2:8 were found to have a mean pore area A_{pore} proportional to $\omega^{-0.42}$ and $\omega^{-0.43}$, respectively, which correlated very well with film thickness. This fitting result indicates that the film thickness as well as the growth of phase separation domains is simultaneously controlled during spin-casting.

The mean pore area A_{pore} and film thickness h are correlated with an exponent close to 1 ($A_{pore} \propto h$). Thus the correlation between pore diameter D_{pore} and thickness is $D_{pore} \propto h^{0.5}$. Meanwhile, the shape and size of PS regions was unchanged before and after solvent etching, which means the PS droplet diameter should satisfy $D_{dp} = D_{pore} \propto h^{0.5}$. Based on our results, the height ratio of PS domain h' to film thickness h is constant at a given blend ratio, namely $h' \propto h$. Therefore, the aspect ratio α, i.e. ratio of the PS droplet diameter D_{dp} to the height of the droplet h', can be obtained as α (D_{dp}/h') $\propto h^{-0.5}$. In the case of a blend ratio of 1:9, the amount of PS was too low and the size of PS droplets was too small to penetrate the entire thickness of the film. By contrast, a blend ratio of 2:8 gave sufficient PS to generate a perforated film. Using the same blend composition, the aspect ratio α becomes smaller with increasing film thickness.

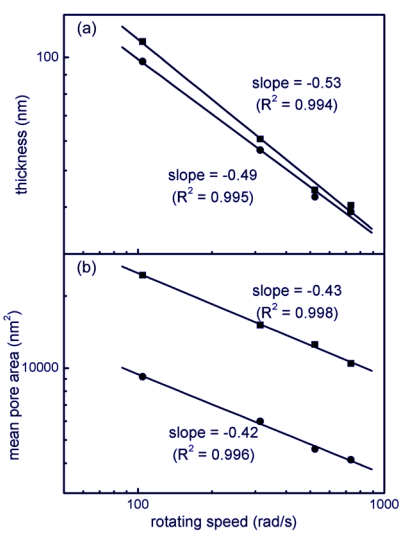

Figure 2-10. Correlation between film thickness and pore size; (a) film thickness versus rotating speed; (b) mean pore area versus rotating speed (circle: 1:9; rectangle: 2:8).

In the case of films with a small α value, the phase separation domains are unstable and tend to break up vertically, generating pores that do not completely penetrate the film. Our results show that in order to prepare a perforated nanoporous thin film, the film thickness ought to be decreased to a level comparable to the dimensional scale of the phase separation domains. Hence, porous films with micron-scale thickness prepared by polymer phase separation are always semi-perforated and the proportion of pores penetrating the film is very limited.

4-4. Phase Separation Mechanism within Blend Ultrathin Films.

In this study, PS and PMMA with various weight ratios were dissolved in CH_2Cl_2 at total polymer concentration of 1.0 wt%. During spin-casting, the T_g change of this ternary system would have a great influence on the evolution of the phase separation and finally determined the morphology of the ultrathin films. In order to estimate the T_g of this polymer blend solution, the Kelley - Bueche equation based on the free volume theory was proposed [13].

$$Tg(\text{system}) = [4.8\times10^{-4}cTg + \alpha_S(1-c)Tg']/[4.8\times10^{-4}c + \alpha_S(1-c)] \quad (2\text{-}5)$$

where c was the volume fraction of polymer in a binary system, T_g (K) and T_g' (K) denoted the glass transition temperature of polymer and solvent, α_S (K^{-1}) was the corresponding thermal expansion coefficient of solvent. In this study, the ternary system was regarded as a binary one for simplicity, since the T_g of PS and PMMA were very close, 100 and 105 °C respectively.

The T_g of polymer was took as 373 K (100 °C) and the volume fraction of polymer was substituted by the weight fraction (1.0 wt% total polymer concentration) for simplicity. The coefficient α_S was usually of the order of 10^{-3} and the particular

value of α_S was of less significance since a change in α_S would merely change the result of calculation. The α_S of CH_2Cl_2 was chosen to be 1.4×10^{-3} K [14] and the T_g' of CH_2Cl_2 was chosen to be 100 K (-173 °C) [15], derived from the literature values.

According to equation (2-5), the T_g of PS/PMMA/CH_2Cl_2 solution at 1.0 wt% total polymer concentration was calculated to be ~101 K (-172 °C). Similarly, when the system reached the T_g of room temperature (25 °C, 298 K), the total polymer concentration was calculated to be ~88.5 wt%, referred to as the vitrification point. It meant that although the solvent kept on evaporating to thin the film after pass through this point, the polymer chains had become a vitrification state and the morphological structures existing at this point had been frozen and would keep the same until the end of spin-casting.

A typical ternary phase diagram for a PS/PMMA/CH_2Cl_2 system (partial enlargement) was shown in Figure 2-11, which was depicted from the previous studies [16]. The accuracy of Figure 2-11 was very limited; however, such a phase diagram was sufficient for discussion of this study. The lines in Figure 2-11 (a) indicated the variation of composition on the path of solvent evaporation of each system, 1:9, 2:8, and 3:7 w/w blend ratios, respectively. It was proposed that the weight ratio of PS to PMMA within the system kept constant during spin-casting. Take the 2:8 w/w blend ratio into account, as shown in Figure 2-11 (b). The point *P* along the path was the composition at which the system entered into the two-phase region and the phase separation initially took place. As the spin-casting proceeded, more CH_2Cl_2 was evaporated, the composition varied from *P* to *P'*, at which the polymer blend solution had spontaneously separated into two phases, a PS-rich phase *Q* and a PMMA-rich phase *Q'* with compositions linked by the tie line. During phase separation process, if the system could maintain the thermodynamic equilibrium all the time, the

composition of PS-rich and PMMA-rich phases could vary along the binodal curve until reaching their vitrification points. However, it was actually seldom to be achieved for some inevitable kinetic barriers.

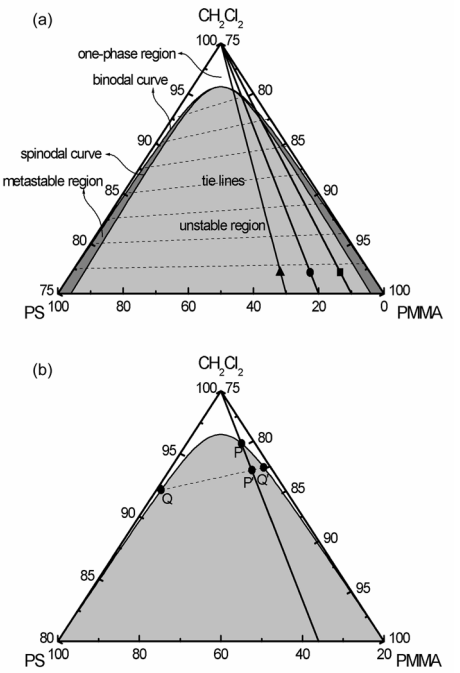

Figure 2-11. Phase diagram for PS/PMMA/CH_2Cl_2 system (partial enlargement); (a) path of solvent evaporation during spin-casting (■ 1:9 w/w, ● 2:8 w/w and ▲ 3:7w/w); (b) path of solvent evaporation during spin-casting of 2:8 w/w in detail.

Two possible mechanisms have to be considered: NG and SD. Which of these two mechanisms controls the phase separation within the ultrathin polymer blend films was unknown. Films prepared with a blend ratio of 2:8 and at a rotating speed of 5000 or 7000 rpm exhibited some irregular structures, as mentioned above. These structures had a characteristic shape and are certainly the vestiges of the bicontinuous

morphology generated by the SD mechanism. Using the lateral profile corresponding to the irregular structures, the author confirmed that immature PS droplets give these irregular structures, though they are still in the process of formation (Figure 2-11). These irregular structures could be deemed to be the result of the transition from a bicontinuous to a dispersed morphology. These observations provide direct evidence that the SD mechanism is preferentially initiated by the rapid quenching during spin-casting.

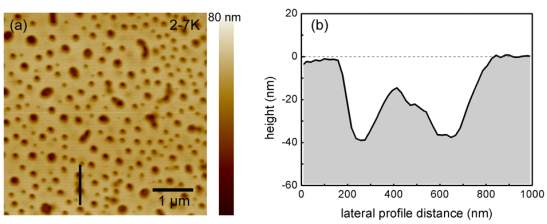

Figure 2-12. AFM height image of a film prepared with 2:8 w/w, 7000 rpm; (a) bottom side after solvent etching; (b) lateral profile drown at the line place shown in (a).

Herein, the author present a simple model for the phase separation mechanism within an ultrathin polymer blend film during spin-casting as outlined in Figure 2-13.

First, a liquid film with uniform thickness tends to form as a result of the balance between centrifugal and viscous forces. With the subsequent solvent evaporation, the polymer concentration gradually increases. When the system enters the two-phase region, phase separation is initiated by fluctuations in concentration, which gives rise to a bicontinuous morphology (Figure 2-13 (a)). The concentration difference and the interstitial space between the two phases increase as the phase separation proceeds. In some cases, the amount of minority component in the blend is insufficient to maintain

a continuous morphology, which subsequently breaks up into numerous irregular structures (Figure 2-13 (b)).

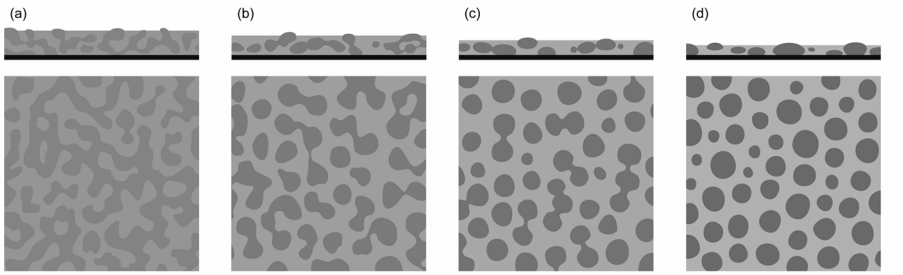

Figure 2-13. Model for the phase separation mechanism within ultrathin blend films during spin-casting; (a) initiated by concentration fluctuations; (b) broken up into irregular structures; (c) formed into flattened droplets; (d) frozen via vitrification (top row: lateral view; bottom row: top view and PS: dark gray; PMMA: light gray).

The concentration difference and the interstitial space between the two phases increase as the phase separation proceeds. In some cases, the amount of minority component in the blend is insufficient to maintain a continuous morphology, which subsequently breaks up into numerous irregular structures (Figure 2-13 (b)). The irregular structures are distributed in a random fashion and spontaneously form spherical shaped droplets in order to minimize the interfacial area with the surrounding milieu. In fact, numerous flattened droplets are present owing to the effect of dimensional confinement within the ultrathin film (Figure 2-13 (c)). The phase separation domains continue to grow by diffusion and coarsening. When the T_g of this polymer-diluent system reaches room temperature, the phase separation stops and the morphological structures are frozen at that time. The final film would be obtained after all the solvent completely evaporated (Figure 2-13 (d)). Therefore, the evolution of the

phase separation morphology within ultrathin polymer blend films was strongly determined by the solvent evaporation rate. For lower rotating speeds, the rate of solvent evaporation is slower, which gives a longer time for a coarsening process. The effect of lowering the solvent evaporation rate is to increase the dimensional scale of the phase separation domains and also the size of the nanopores. The ultrathin films prepared with a blend ratio of 3:7 generated more obvious morphological features that illustrate this point (Figure 2-14).

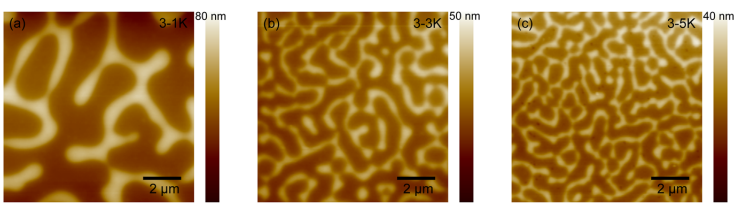

Figure 2-14. AFM height images of as-cast films prepared with 3:7 w/w; (a) 1000 rpm; (b) 3000 rpm and (c) 5000 rpm.

5. Summary

Ultrathin films with nanostructures were prepared by spin-casting an immiscible polymer blend, PS/PMMA. For some blend ratios, the nanoporous structure was observed after solvent etching. The author demonstrated that when the thickness of ultrathin film is comparable to the dimensional scale of the phase separation domains, it is feasible to prepare perforated ultrathin films with nanopores in the range of tens of nanometers. A simple model was proposed for the phase separation mechanism within ultrathin films during spin-casting, illustrating that the spinodal decomposition mechanism plays an important role in determining the final morphology.

References

1. N.A. Kotov *et al*., *Langmuir*, 2000, 16, 5530.

2. V.V. Tsukruk *et al*., *Adv. Mater.*, 2004, 16, 157.

3. S. Walheim *et al*., *Macromolecules*, 1997, 30, 4995.

4. D.P. Birnie, *J. Mater. Res.*, 2001, 16, 1145.

5. S. Takeoka *et al*., *Adv. Mater*., 2007, 19, 3549.

6. S. Takeoka *et al*., *Adv. Funct. Mater.*, 2009, 19, 2560.

7. S. Takeoka *et al*., *Adv. Mater.*, 2009, 21, 4388.

8. S. Takeoka *et al*., *Biomaterials*, 2010, 31, 6269.

9. D.K. Owens *et al*., *Appl. Polymer Sci.*, 1969, 13, 1741.

10. A. Mas *et al*, *Polym. Int.*, 2003, 52, 1222.

11. D.E. Bornside *et al*., *J. Imaging Technol.*, 1987, 13, 122.

12. D. Meyerhofer, *J. Appl. Phys.*, 1978, 49, 3993.

13. F.N. Kelley *et al*., *J. Polym. Sci.*, 1961, 50, 549.

14. D.R. Lide, *CRC Handbook of Chemistry and Physics*, Taylor and Francis, 2007.

15. R.F. Fedors, *J. Polym. Sci. Polym. Lett. Ed.*, 1979, 17, 719.

16. L. Lin *et al*., *Langmuir*, 1994, 10, 2495.

Chapter 3

Construction of Porous Polymer Ultrathin Films and their Potential Uses in Bioapplication

1. Introduction

2. Construction of Porous Polymer Ultrathin Films

3. Potential Uses of Porous Ultrathin Films in Bioapplication

4. Summary

References

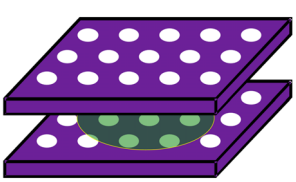

1. Introduction

The ultimate goal of this study is to construct polymer ultrathin films to be applied as a model to mimic the diversity of complex biosystems. Therefore, methodology of construction method should be essentially a generalized method.

In this chapter, the author developed a series of simple and fast methods to prepare polymer ultrathin film with porous structures. The methodology presented in this study was proven as an effective and versatile way to acquire various nanostructures. Regarding to the application of the porous structure within the polymer ultrathin film, some potential possibilities were also proposed and discussed.

2. Construction of Porous Polymer Ultrathin Films

2-1. Nanoparticle-patterned Substrate System

The polymer and nanoparticle used in this study were poly(lactic acid) (PLA) (*Mw* = 300,000; *Mw*/*Mn* = 1.8; d = 1.25 g/cm^3) and Polybead Microspheres (diameter = ~900 nm, density = 2.66 wt%), which were purchased form Polysciences, Inc. (Warrington, PA). Water-soluble poly(acrylic acid) (PAA) (*Mw* = ~250,000) used for preparing a sacrificial layer was purchased form Kanto Chemicals Co., Inc. (Tokyo, Japan). The spin-casting substrates used in this study were silicon (100) wafers covered with 200 nm thermally grown silicon oxide (SiO*x*), as mentioned above.

PAA was dissolved in water with concentration of 8.5 wt%. Then nanoparticles dispersion liquid was mixed with PAA aqueous solution with volume ratio of 5:95. The nanoparticle-patterned sacrificial substrate was prepared by spin-casting at various rotating speeds (1000, 2000, 3000, 5000, and 7000 rpm) for 60 s. PLA solution was prepared in acetic acid with concentration of 3.0 wt% and was dropped onto this nanoparticle-patterned sacrificial substrate and spin-casted at 3000 rpm for 60 s.

Finally, the as-cast films were immersed into deionized water. By the dissolution of the underlying PAA sacrificial layer, the resulting film could be detached from the silicon substrate and sustain their shape on the water surface. Furthermore, nanoparticles can be washed out during freestanding process, which induced the formation of polymer ultrathin films with uniform pores (Figure 3-1).

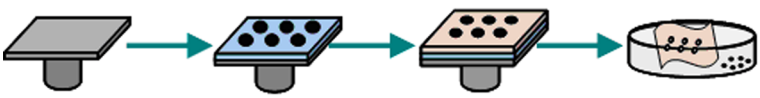

Figure 3-1. Illustration of construction porous polymer ultrathin films by nanoparticle-patterned substrate method.

Figure 3-2 (a) and (b) represented typical *in situ* AFM images taken before and after PLA coating. It was obvious to see that the protrusion domains corresponded to nanoparticles with height of ~900 nm (Figure 3-2 (a1) and (b1)). After PLA coating, there found no morphological differences before and after solvent etching, but the height difference between protrusion domains and film surface was decrease, indicating the existence of PLA ultrathin film (Figure 3-2 (a2) and (b2)), indicating the thickness of PLA films were ~200 nm. Figure 3-2 (a3) and (b3) profile was drawn at the same place of Figure 3-2 (a) and (b) and displayed together.

The author then investigated how certain preparation conditions influenced the porous structure after spin-casting. AFM images of four typical samples prepared at various rotating speeds (1000, 2000, 3000, and 5000 rpm) are shown in Figure 3-3. During freestanding process, all of the nanoparticles were washed out and gave a uniform porous morphology, somewhat equal to the size of nanoparticle ~900 nm. Owing to the diameter of nanoparticle used in this study was larger than the total

thickness of PAA sacrificial and PLA ultrathin film composite, there is no doubt that these pores indeed penetrate the entire thickness of the film.

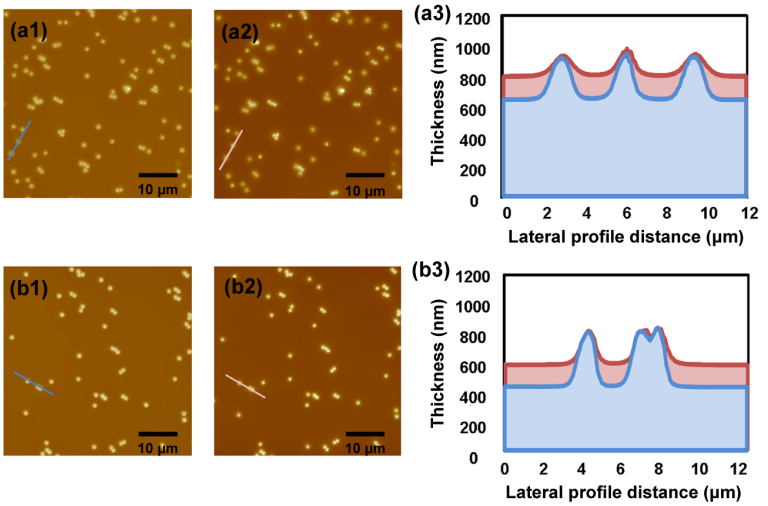

Figure 3-2. *In situ* AFM height images of a PLA film on nanoparticle-patterned sacrificial substrate prepared at (a) 3000 and (b) 7000 rpm. (a1) and (b1) before PLA coating, (a2) and (b2) after PLA coating, (a3) and (b3) lateral profile drawn at the line places shown in (a), (b) and displayed together (before: blue; after: pink).

As the rotating speed increased, the total number of nanoparticle in the area of the AFM image (50 × 50 μm^2), also called pore density was decreased. The analyses results were listed in Table 3-1. The author proved by using this method, one can prepare porous ultrathin film with narrow pore size distribution, and simultaneity, the pore density can be easily performed in a controllable manner.

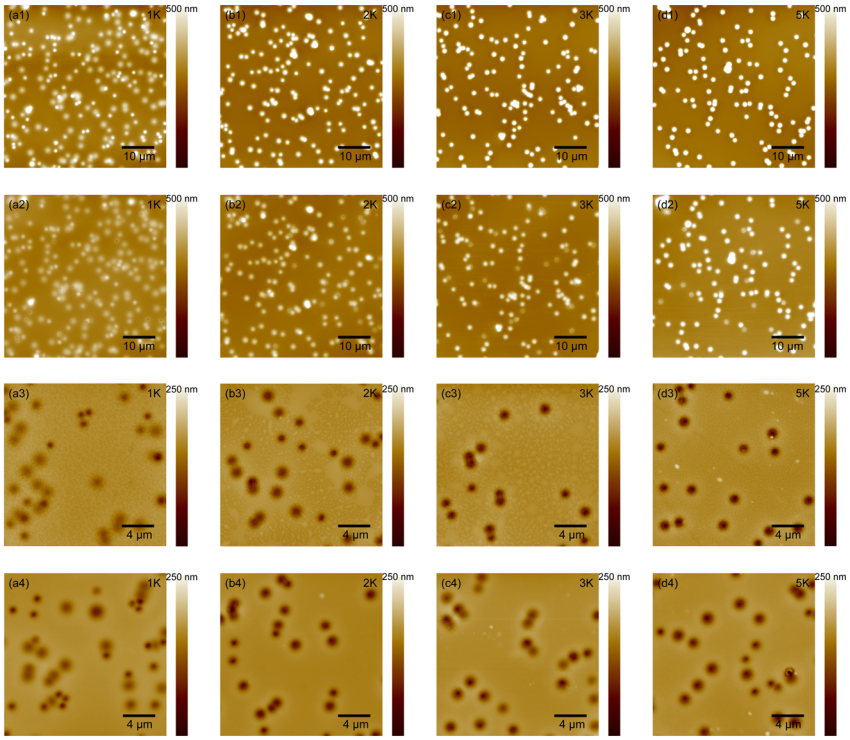

Figure 3-3. AFM height images of PLA film prepared by nanoparticle-patterned substrate method; before PLA coating (first row), after PLA coating (second row), top side after freestanding (third row), and bottom side after freestanding (forth row) for 1000 rpm (first column), 2000 rpm (second column), 3000 rpm (third column) and 5000 rpm (forth column).

Table 3-1. Measures of porous PLA film prepared by nanoparticle-patterned substrate method.

Sample (rpm)	Patterned substrate thickness (nm)	Pore diameter (μm)	Pore density (10^{-3}/μm^2)
1000	1043.0 ± 12.4	0.9 ± 0.4	82.5
2000	782.0 ± 18.2	0.9 ± 0.2	55.3
3000	642.2 ± 22.8	0.9 ± 0.4	51.0
5000	533.7 ± 24.3	0.9 ± 0.3	47.5
7000	445.8 ± 23.3	0.9 ± 0.4	44.3

2-2. Polymer - Polymer Blend System

In chapter 2, the author has demonstrated that when the thickness of ultrathin film is comparable to the dimensional scale of the polymer blend phase separation domains, typically less than half of the diameter of the PS droplets, it is feasible to prepare perforated ultrathin films with nanopores. Herein, the author extended this study and generalized the corresponding method to biocompatible polymer for expanding the potential uses in bioapplication. The polymers used were PS and PLA. PVA was chosen for preparing sacrificial layer. The spin-casting substrates and all materials have been mentioned above and kept the same as the previous studies.

Polymer blend solution was prepared by dissolving PS and PLA with weight ratio of 3:7 in analytic grade ethyl acetate as common solvent, and was stirred overnight prior to film preparation in order to ensure complete dissolution.. The total polymer concentration in the solutions was 1.0 wt%. Spin-casting was performed onto a PVA-coated substrate at various rotating speeds (1000, 3000, 5000, and 7000 rpm) for 60 s. The as-cast blend films were immersed into cyclohexane to selectively remove the PS regions and leave the PLA porous film. Furthermore, the freestanding state of porous can also be obtained (Figure 3-4).

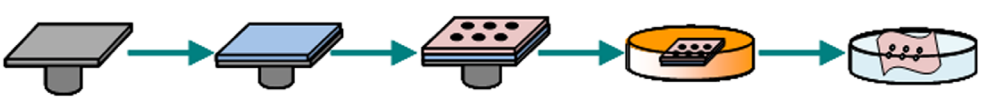

Figure 3-4. Illustration of construction porous polymer ultrathin films by polymer - polymer blend method.

Figure 3-5 shows the phase separation morphology obtained from numerous PS droplets embedded in matrix of PLA. By immersing an as-cast blend film into

cyclohexane overnight, PS regions were removed to prepare nanopores. As to the question whether these pores can penetrate the entire thickness of the film, SEM was applied to observe the surface of the resulting porous PLA film (Figure 3-6). As the rotating speed increased, the size of the pore becomes smaller, while the pore density was increased, which coincides with the previous study in chapter 1 (Table 3-2).

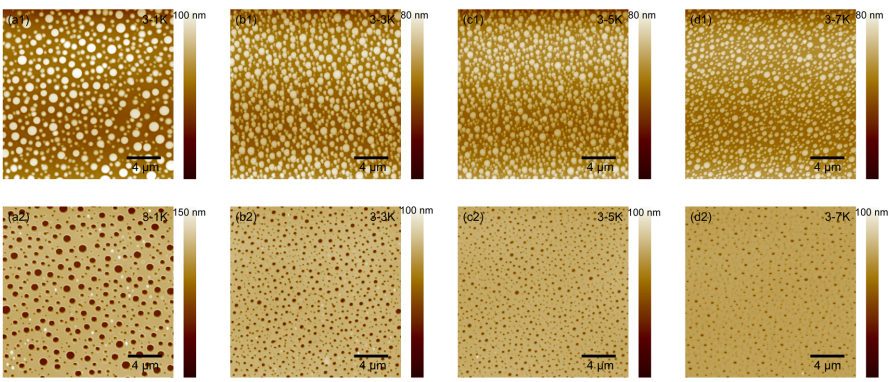

Figure 3-5. AFM height images of PLA film prepared by polymer - polymer blend method; before solvent etching (top row), after solvent etching (bottom row) for 1000 rpm (first column), 3000 rpm (second column), 5000 rpm (third column) and 7000 rpm (forth column).

Different from PS/PMMA blend with 3:7 blend ratio in chapter 1, the morphology of PS/PLA blend with 3:7 blend ratio shows island-like morphology, which indicates a more adequate evolution of phase separation. As a result, relatively larger porous structures were obtained, in this case from ~200 to ~500 nm, whereas the film thickness is quite ultrathin, from ~25 to ~75 nm, much less than half of the diameter of PS domains. The SEM observations supported this in a compelling way. In all cases, the resulting films were found to be perforated even with the lowest solvent

evaporation rate and relatively thick thickness, namely, 1000 rpm and ~75 nm.

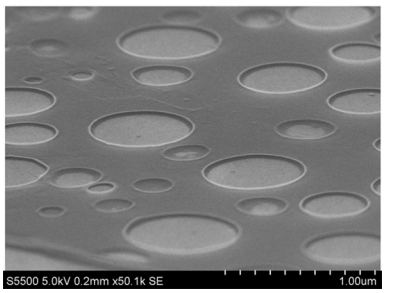

Figure 3-6. Surface SEM for PLA film prepared by polymer - polymer blend method at 1000 rpm.

Table 3-2. Measures of porous PLA film prepared by polymer - polymer blend method.

Sample (rpm)	thickness (nm)	Pore diameter (μm)	Pore density (/μm^2)
1000	76.8 ± 2.3	0.49 ± 0.24	1.2
3000	40.8 ± 2.6	0.33 ± 0.15	2.4
5000	32.6 ± 1.3	0.24 ± 0.10	2.7
7000	26.2 ± 0.8	0.23 ± 0.11	2.9

2-3. Polymer - Inorganic Salt Blend System

Except for polymer - polymer phase separation, the author explored the possibility of more simple and fast bottom-up methods to prepare polymer ultrathin film with porous structures. It is reasonable to suppose that the phase separation between polymer and inorganic salt will be more intense and adequate compared with polymer - polymer blend system. Furthermore, most inorganic salts are water-soluble, which means after phase separation, the inorganic salt domains can be easily washed out by water during freestanding process, without necessary to perform an extra selective solvent etching process. The author calls it as a one-step method.

The polymer used was PLA and PVA was chosen for preparing sacrificial layer. The spin-casting substrates and all materials have been mentioned above and kept the same as the previous studies. Herein, lithium bromide (LiBr) was used as a model inorganic salt to mix with PLA. Its extreme solubility makes LiBr hygroscopic in air. Therefore, before use LiBr was fully drying at 150 °C ant quickly dissolved in ethyl acetate with concentration of 6.0 wt%. PLA was dissolved in ethyl acetate with the concentration of 3.0 wt%. Then these two solutions were mixed with each other with various volume blend ratio (10:1, 10:2, 10:3, 10:4, and 10:5 v/v). Spin-casting was performed onto a PVA-coated substrate at 3000 rpm for 60 s (Figure 3-7).

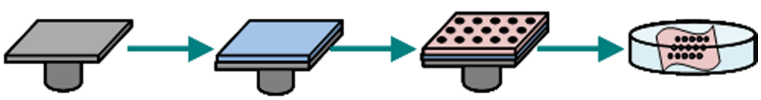

Figure 3-7. Illustration of construction porous polymer ultrathin films by polymer - inorganic salt blend method.

Figure 3-8 shows the phase separation morphology obtained from numerous quasi- sphere LiBr crystals embedded in matrix of PLA after spin-casting. With increasing the amount LiBr in the blend system, both of the total area and the density of LiBr domains were increased, accompanied with the increased surface roughness. After freestanding process, namely to immerse the as-cast films into water, all LiBr was quickly dissolved in water and induce the formation of the porous structure. With no doubt, the microscale pores can penetrate the entire thickness of the film, whereas a number of small pores were semi-opened. For example, a typical SEM image shows a small pore with diameter of ~600 nm cannot penetrate ~ 300 nm film (Figure 3-9).

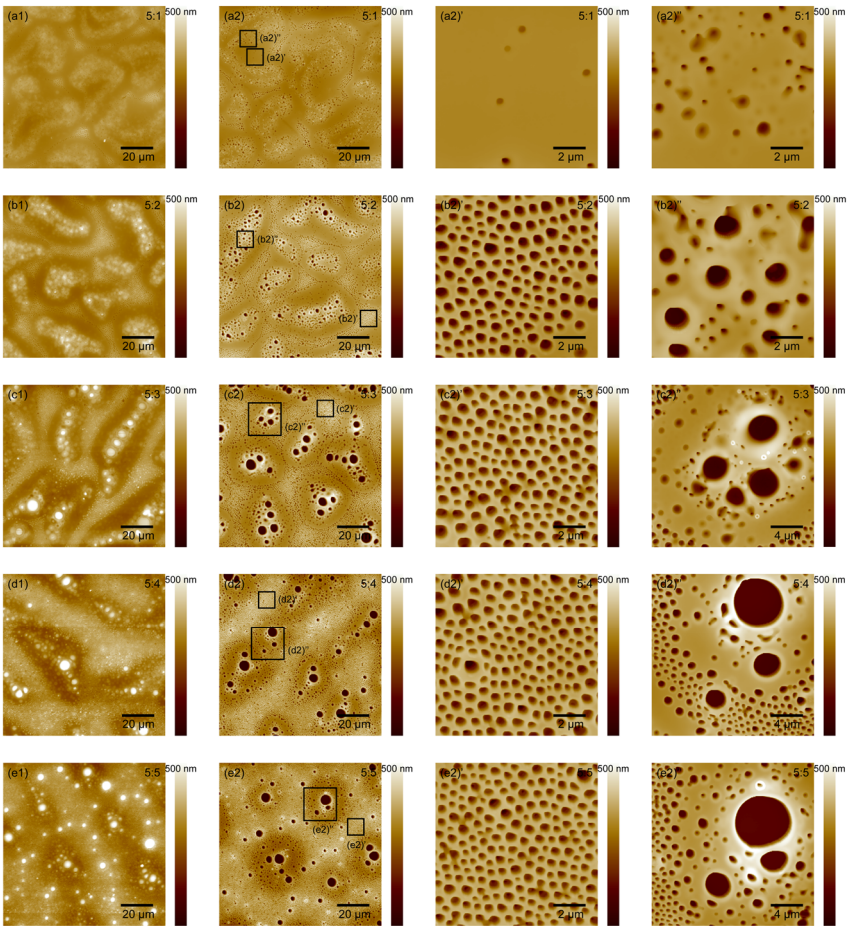

Figure 3-8. AFM height images of PLA film prepared by polymer - inorganic salt blend method; blend ratio of 10:1 (first row), blend ratio of 10:2 (second row), blend ratio of 10:3 (third row), blend ratio of 10:4 (forth row), and blend ratio of 10:5 (fifth row) for as-cast films (first column) and after freestanding (second column), enlarged images at the corresponding regions shown in the third and the forth column.

With increasing the amount of LiBr in blend system, film thickness was almost kept constant ~300 nm as blend ratio has little influence on viscosity in this case. However, the average pore diameter and pore density were increased from ~ 500 to

~600 nm and from 0.37 to 2.04 /μm^2, respectively. The distinct of this polymer - inorganic salt blend method , as shown in Figure 3-8, is that the pore size distribution is unfavorable large with increasing the amount of inorganic salt. The author reasoned that owing to an intense phase separation, the concentration fluctuation was induced and the crystallization behavior of inorganic salt became locally heterogeneous and difficult to be controlled. Although that, this method provide a possibility of simple and fast bottom-up methods to prepare polymer ultrathin film with porous structures.

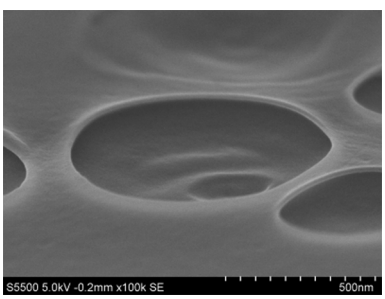

Figure 3-9. Surface SEM for PLA film prepared by inorganic salt with blend ratio of 10:5 v/v.

Table 3-3. Measures of porous PLA film prepared by polymer - inorganic salt blend method.

Blend ratio (v/v)	thickness (nm)	Pore diameter (μm)	Pore density (/μm^2)
10:1	283.0 ± 23.3	0.50 ± 0.22	0.37
10:2	275.8 ± 46.9	0.59 ± 0.44	1.53
10:3	262.8 ± 28.7	0.51 ± 0.61	1.77
10:4	282.2 ± 76.3	0.60 ± 0.52	1.84
10:5	271.8 ± 98.2	0.59 ± 0.63	2.04

2-4. Polymer - Solvent - Poor Solvent System

The effect of solvent on polymer phase separation is significantly important [1-3]. A typical ternary phase diagram for polymer - solvent - poor solvent was shown as

Figure 3-10. It is obvious to see that the point C along the path was the composition at which the system entered into the two-phase region and the phase separation initially took place. In the case of path 1, a dense homogeneous glass polymer film will be prepared without phase separation. In the case of path 2, NG mechanism controls the phase separation and exhibit dispersed morphology. In the case of path 3, SD mechanism is predominated and induces bicontinuous morphology.

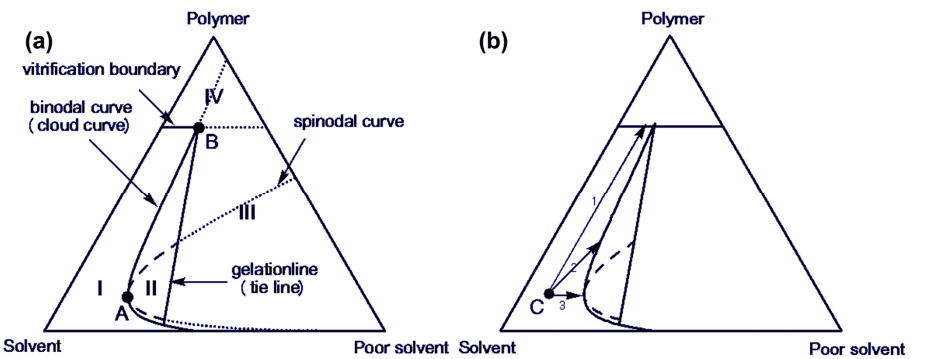

Figure 3-10. Typical phase diagram for amorphous polymer – solvent - poor solvent; (a) I region: homogeneous liquid state, II region: liquid-liquid two-phase state, III region: liquid-glass two-phase state, IV region: glass state, Point A: critical point, Point B: Berghmans's point, (b) Point C: initial composition of casting solution.

The polymer used was PLA and PVA was chosen for preparing sacrificial layer. The spin-casting substrates and all materials have been mentioned above and kept the same as the previous studies. Ethyl acetate and dimethyl sulfoxide (DMSO) were used as solvent and poor solvent respectively and mixed with various volume blend ratio (100:1, 100:3, and 100:5). PLA was dissolved in this mixed solvent with the concentration of 3.0 wt%. Spin-casting was performed onto a PVA-coated substrate at various rotating speeds (1000, 3000, and 5000 rpm) for 60 s. The as-cast films

exhibited porous structures, without need of subsequent solvent etching process (Figure 3-11). Therefore, the author also calls this method as a one-step method.

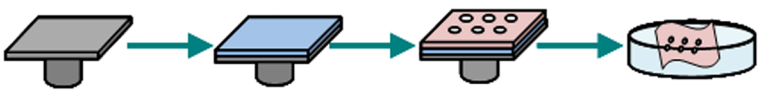

Figure 3-11. Illustration of construction porous polymer ultrathin films by polymer - solvent - poor solvent method.

Compared with ethyl acetate, whose boiling point at 1 atm is 77.1 °C, the boiling point of the poor solvent DMSO is much higher (189.0 °C). This induced the relatively slow evaporation speed and liquid-liquid phase separation with PLA rich phase. After the ethyl acetate and DMSO were evaporated completely, the porous structures were obtained. Figure 3-12 shows the resulting morphology by adjusting the preparation conditions, including blend ratio of mixed solvent and rotating speed. It has been proved that the porous could be fabricated conveniently by this one-step method, and a perforated film with pore size of several micrometers was achieved in this study.

Similar to the case of polymer - polymer blend method, SEM was applied to observe the surface of the resulting porous PLA film and found that in all cases the resulting films were indeed perforated (Figure 3-13). However, the morphologies of top and bottom side of film show somewhat different, namely the pore density derived from top side is significantly higher that that derived from the bottom side. This is interpreted by the evaporation process prominently happened at the top side of a film and there exist the DMSO concentration gradation within the vertical direction of the film. The diameter of pores was dramatically influenced by mixed solvent blend ratio, namely with increasing the amount of poor solvent, porous structure are more obvious

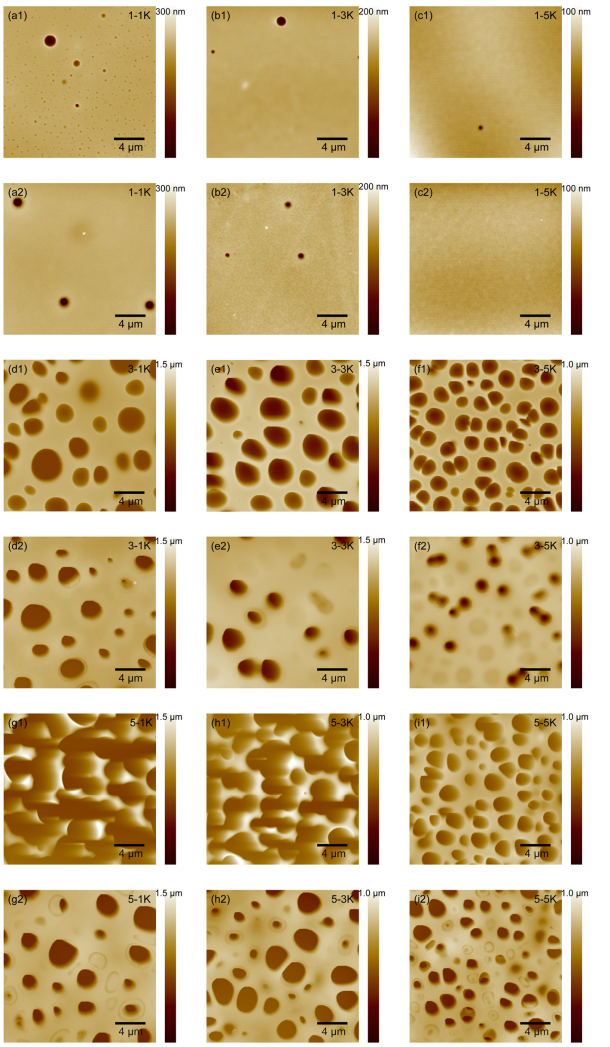

Figure 3-12. AFM height images of PLA film prepared by polymer - solvent - poor solvent method; top side of 100:1 (first row), bottom side of 100:1 (second row), top side of 100:3 (third row), bottom side of 100:3 (forth row), top side of 100:5 (fifth row), and bottom side of 100:5 (sixth row) for 1000 rpm (first column), 3000 rpm (second column), and 5000 rpm (third column).

as shown in Figure 3-12. With the same rotating speed, increased blend ratio gives increased thickness of the resulting film, which was interpreted that the viscosity of mixed solvent increased by increasing amount of DMSO. The kinetic viscosity at 20 °C of ethyl acetate and DMSO are 0.408 and 2.200 mPa s, respectively. With the same blend ratio, as the rotating speed increased, the size of the pore becomes smaller, while the pore density was increased, which coincides with the previous study (Table 3-4).

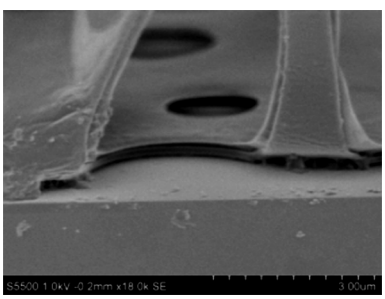

Figure 3-13. Surface SEM for PLA film prepared with 100:3 mixed solvent and at 1000 rpm.

Table 3-4. Measures of porous PLA film prepared by polymer - solvent - poor solvent method. [a]

Preparation conditions	thickness (nm)	Pore diameter (μm)	Pore density (10^{-3}/μm^2)
100:1 v/v; 3000 rpm	275.1 ± 17.7	0.6 ± 0.3	8.8
100:3 v/v; 3000 rpm	296.8 ± 18.0	1.8 ± 1.1	90.0
100:5 v/v; 3000 rpm	413.8 ± 31.3	n.d.	n.d.
100:3 v/v; 1000 rpm	583.8 ± 48.8	2.1 ± 1.0	75.0
100:3 v/v; 5000 rpm	241.0 ± 18.4	1.6 ± 0.6	107.5

[a] The samples prepared with 100:5 v/v mixed solvent blend ratio at 3000 rpm gave bicontinuous morphology; therefore, the porous information was not listed here.

3. Potential Uses of Porous Ultrathin Films in Bioapplication

3-1. Optical Properties of Porous Ultrathin Films and Application

The film opacity is related to the ability of light to pass through the film, it describes the absorption and scattering of visible light. The polymer ultrathin films with nanostructures prepared in this study are essentially opaque and cloudy owing to light scattering by rough film surface, whereas the homopolymer featureless polymer ultrathin films are always transparent. For example, the porous structures contain light scattering voids that enhance the optical absorption [4].

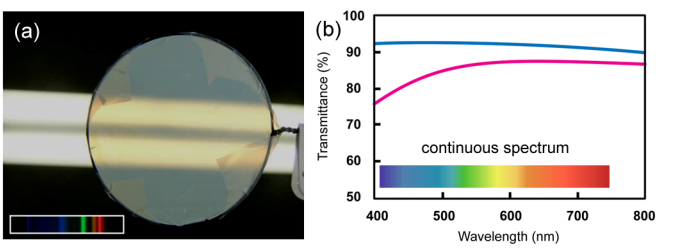

Figure 3-14. Observation of ultrathin film opacity. (a) Opaque ultrathin film supported by a wire loop with a daylight tube as background. (b) Visible light transmittance versus wavelength of microscope glass slides that were covered with nanoporous ultrathin film. Cyan: blank control of a glass slide, red: glass slide covered with nanoporous ultrathin film.

As shown in Figure 3-14, a typical sample prepared in this study was freestanding and carefully supported by a wire loop. The film appeared opaque and cloudy in visual observation. By the help of a daylight tube as background, the transmitted light shows an orange color, which implied that the component of blue and purple wavelength on the spectrum have been somewhat absorbed by the porous film. It is noted to be mentioned that the spectrum of daylight tube is line spectra, as shown inset Figure

3-14 (a). As a continuous spectrum source, uv-visible spectroscopy was used to study the optical properties of porous ultrathin films. With the same sample, the transmittance of glass slides that were covered with nanoporous ultrathin film was decreased as least ~15 % in the range of blue and purple wavelength on the spectrum, compared to bare glass (Figure 3-14 (b)). This result agreed with the visual observation very well. The sample presented here is a PLA porous film prepared by polymer - solvent - poor solvent method. The thickness of the film is ~300 nm and the average diameter of pore is ~1.8 μm.

Regarding to the application of optical properties of porous ultrathin films, some attempts have been tried and in process at present. In the previous studies, it has been proved that the freestanding method is an efficient means of transferring the ultrathin film from solid substrate to various other surfaces, such as human skin, which would enlarge the potential of its uses. The author have planed to develop a new cosmetic product as eye patch by using porous ultrathin films, which was expect to play a practical role in concealing the wrinkle or the fleck on one's face.

3-2. Biocompatible Polymer Porous Ultrathin Films as Filter Membrane

As to a porous film, the most stirring application field maybe the filtration process and porous film is utilized as a filter membrane. As mentioned above, the biocompatible PLA base porous films were prepared by various construction methods. The thickness of the films could be adjusted in the range from ~25 to ~600 nm and the diameter of porous structures with controllable density and distribution from tens of nanometer to microscale have been fabricated. It is reasonable to suppose that the polymer ultrathin film with nanopores would be a good candidate for filter membrane.

Figure 3-15 is an illustration of various types of membrane process, which shows the particular application scope and the corresponding pore size. In order to separate the protein like macromolecule and microorganisms, the porous structure must be in the range from tens of nanometer to microscale. Similar to this range, the author framed the range of diameter of pore that can be possible prepared in this study, as shown in Figure 3-15. Therefore, it is essentially feasible to use polymer porous ultrathin films as filter membrane.

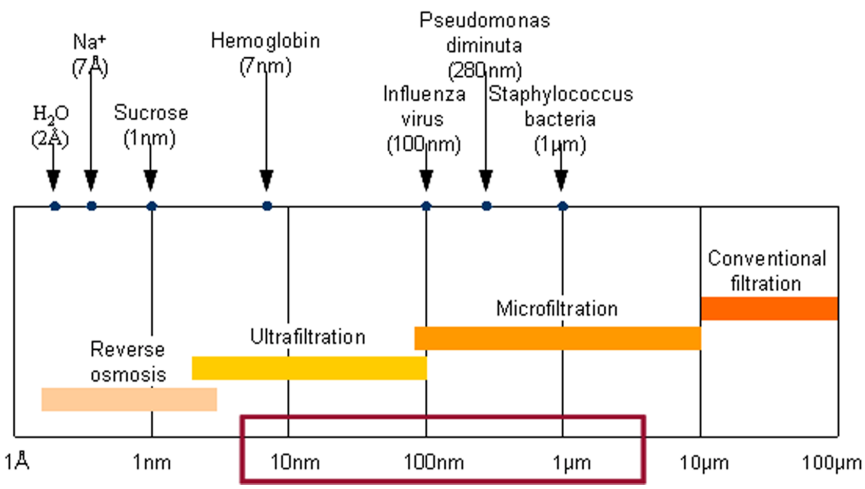

Figure 3-15. Illustration of various types of membrane process (depicted from []).

By combined with the basic principle of a membrane process, transportion through the membrane takes places as a result of driving force acting on the components in the feed [5] (Figure 3-16). In most cases, the permeation rate through the membrane, also called flux, is proportional to the driving force but inversely proportional to the thickness of the membrane, namely the transport barrier, written as

$$J(flux) = -A\frac{dX}{dh} \quad (3\text{-}1)$$

where A is the phenomenological coefficient, X is the driving force such as pressure or concentration difference perpendicular to the membrane thickness h. In using such equation, in order to increase the flux, it is requested to increase driving force or decrease membrane thickness. In the case of a biofilter process, high driving force is always impossible due to the fragile features of biomacromolecules, gentle process required *in vitro* even *in vivo*, which exhibits the potential advantages of using polymer porous ultrathin films as filter membrane. Therefore, the author designs two biofilter models for this purpose.

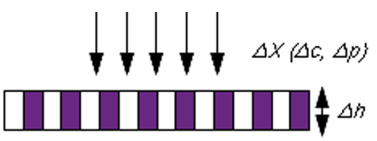

Figure 3-16. Illustration of a model membrane process.

Figure 3-17 shows an *in vitro* biofilter, which performed as protein purification or a virus filtration. The feed in the inner is a mixture of proteins with different dimensional size and outer is phosphate buffered saline (PBS). The polymer ultrathin film is used as filter membrane fixed at the interface. It is supposed that small proteins would pass through the membrane until equilibrium and get concentrated to some extent, whereas big proteins or viruses are withheld in the inner.

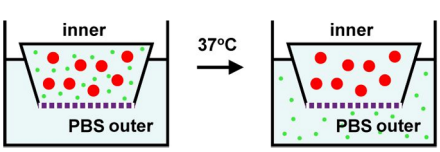

Figure 3-17. Design of protein purification and virus filtration.

Figure 3-18 shows an *in vivo* biofilter, which performed as an immunoisolation device. The design is based on the concept of bioartificial pancreas (BAP), which is a device that consists of encapsulating glucose-responsive insulin-secreting cells and implant into human body as an ideal treatment for diabetes. The immunoisolation system is designed to permeate substances that are essential for the cells to survive and function, such as nutrients and oxygen but not to penetrate cells, antibodies, and complements. The previous studies have proved that biocompatible polymer ultrathin films show advantages as cell culture substrate. Herein, the author wonders if it is possible to culture cells inside the close space constructed by porous polymer ultrathin films. If this hypothesis can be proved workable, the polymer porous ultrathin film would become a good candidate to be used as immunoisolation device *in vivo* study.

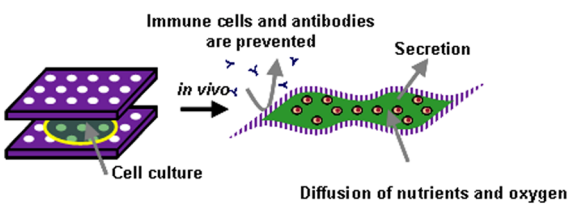

Figure 3-18. Design of immunoisolation device *in vivo* study.

4. Summary

A serious of biocompatible PLA based porous films were prepared by various construction methods, including nanoparticle-patterned substrate method, polymer - polymer blend method, polymer - inorganic salt blend method, and polymer - solvent - poor solvent method. The shape, size, density, aspect ratio and even the proportion of nanostructures penetrating the film could be easily controlled by these methods.

References

1. P. Vandewitte *et al*., *J. Controlled Release*, 1993, 24, 61.

2. S.G. Li *et al*., *Macromolecules*, 1996, 29, 2053.

3. S. Altinkaya *et al*., *J. Membr. Sci.*, 2005, 249, 163.

4. S. Walheim *et al*., *Science*, 1999, 283, 520.

5. M. Mulder, *Basic Principles of Membrane Technology*, Kluwer Academic Publishers, 1996.

Chapter 4

Evaluation of Tapping Mode Atomic Force Microscopy Tip-Sample Interaction

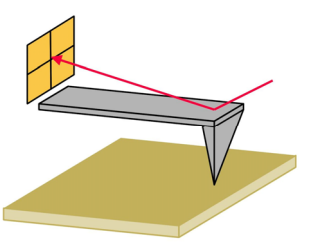

1. Introduction

Atomic force microscopy (AFM) is a versatile and widely used method for imaging polymer surface as well as other soft matter, including biomacromolecules, which has shown its predominance in the study field of soft matter.

In this chapter, the author discussed the basic principles of tapping mode AFM and introduced a technique to confirm the energy dissipation between tip-sample interaction during AFM scanning.

2. Fundamental Aspects of Atomic Force Microscopy

2-1. Concept of Atomic Force Microscopy

Atomic force microscopy, as a powerful tool for characterization of the structure and properties of solid surface, has aroused wide interest. Compared to optical microscopy, scanning electron microscopy, etc., the AFM belongs to a family of scanning probe microscopy (SPM) that is capable of observing sample surface on the nanoscale. The first AFM was developed by G. Binnig *et al*. by gluing a tiny shard of diamond onto one end of a tiny strip of gold foil [1, 2]. Nowadays, AFM can image surface of material in atomic resolution and also measure force at the nanoscale.

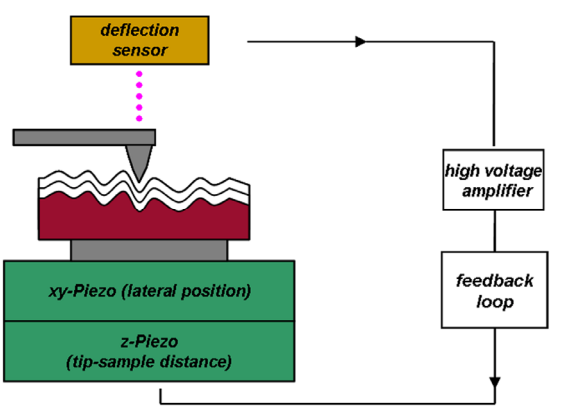

Figure 4-1. Illustration of basic principle of tapping mode AFM.

There are two operation modes in AFM [3]. In contact mode, the tip touches the surface and moved across it during scanning. In tapping mode, the tip is vibrated so that it repeatedly makes contact with the surface. The applied load from operating AFM in contact mode always produces large lateral force to induce surface damage. Thus, in order to avoid deformation, it is more sensible to use tapping mode AFM when scanning is performed on soft matter, such as polymer and biomacromolecule. The basic principle of tapping mode AFM is shown in Figure 4-1.

2-2. Operation Conditions of Tapping Mode Atomic Force Microscopy

In amplitude modulated tapping mode, the tip is excited by an external signal at a frequency close to its resonance value with free amplitude. The frequency, amplitude, and phase of tip change due to the tip-sample interaction. The cantilever is then brought close to the sample surface until the amplitude reaches a given set-point value. In general, imaging was performed while the amplitude is kept constant by feedback loop. A number of scan parameters can be controlled in tapping mode AFM, such as set-point, drive amplitude, and drive frequency.

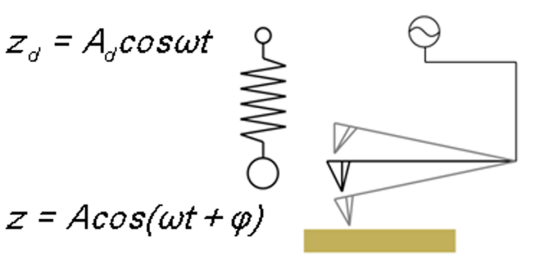

Figure 4-2. Illustration of simple harmonic oscillator model for tapping mode AFM.

By modeling the cantilever as a harmonic oscillator, a theoretical study would help us to have a good understanding on dynamics of tip motion [4] (Figure 4-2).

Equation of a free cantilever motion can be written as

$$m\frac{d^2z}{dt^2} = -b\frac{dz}{dt} - k(z - z_d) \quad (4\text{-}1)$$

$$\omega_0^2 = \frac{k}{m} \qquad Q \equiv \frac{k}{\omega_0 b} \quad (4\text{-}2)$$

By solving equation above, expressions of amplitude and phase can be calculated by

$$A = \frac{A_d\omega_0^2}{\sqrt{(\omega_0^2 - \omega^2)^2 + (\omega\omega_0/Q)^2}}; \tan\varphi = \frac{\omega\omega_0/Q}{\omega_0^2 - \omega^2} \quad (4\text{-}3)$$

In the presence of tip-sample interaction, namely the external force, F_{ext}, equation (4-1) can be modified written as

$$m\frac{d^2z}{dt^2} = -b\frac{dz}{dt} - k(z - z_d) + F_{ext} \quad (4\text{-}4)$$

Tip-sample interaction influences the resonance frequency and spring constant of a cantilever as

$$\omega' = \omega_0 + \Delta\omega \; ; \; k' = k_0 + \Delta k \quad (4\text{-}5)$$

And the frequency shift and the spring constant shift can be related as [5]

$$k' = k - \frac{dF_{ext}}{dz} = k + \frac{2k(\omega_0' - \omega_0)}{\omega_0} \quad (4\text{-}6)$$

By solving equation above, expressions of amplitude and phase can be calculated by

$$A' = \frac{A_d\omega_0^2}{\sqrt{(\omega_0'^2 - \omega^2)^2 + (\omega\omega_0/Q)^2}}; \tan\varphi' = \frac{\omega\omega_0'/Q}{\omega_0'^2 - \omega^2} \quad (4\text{-}7)$$

where the abbreviations used were listed as below. b: viscous constant; k: tip spring

constant; k': modified tip spring constant; m: body mass; φ: phase shift; ω: drive frequency; ω_0: resonance frequency; ω_0': modified resonance frequency; A: tip amplitude; A_d: drive amplitude; and Q: quality factor.

By comparing between the equations (4-1) and (4-7), it was concluded that amplitude, resonant frequency and phase are dramatically affected by force gradient of tip-sample interaction, which can be written as

$$\Delta A(\omega_0) = -\frac{F'^2_{ext}}{2k^2} Q^2 A \qquad \Delta\varphi(\omega_0) = \frac{Q}{k} F'_{ext} \qquad (4\text{-}8)$$

Based on the analyses above, an illustration was drawn as shown in Figure 4-3. In tapping mode AFM, when the tip operated and interacted with sample surface in the attractive region, namely the attractive force dominates the scanning, the resonance frequency will decrease and the phase shift will be lager than 90° compared to the free cantilever. And *vice versa*, when the tip operated and interacted with sample surface in the repulsive region, namely the repulsive force dominates the scanning, the resonance frequency will increase and the phase shift will be smaller than 90° compared to the free cantilever. Furthermore, the repulsive force gradient is essentially greater than that of attractive force, such as van der Waals force as a typical short range force, to operate AFM in repulsive bring more sensitive amplitude response. Therefore, tapping mode AFM is always operated in repulsive region.

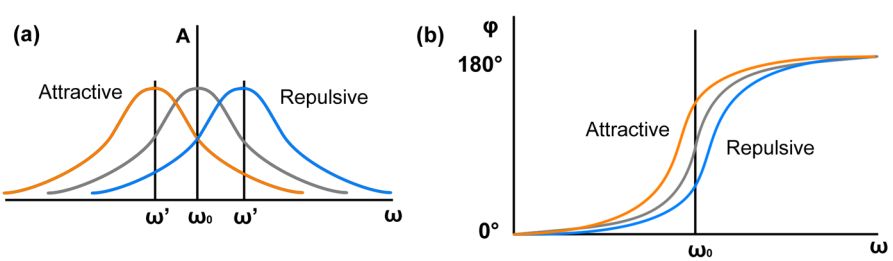

Figure 4-3. Illustration of tip motion in the present of tip-sample interaction.

3. Evaluation of Tip-Sample Interaction in Tapping Mode AFM

3-1. Determination of Imaging Force in Tapping Mode AFM

In order to obtain a deeper understanding about tip-sample interaction in tapping mode AFM, it is necessary to determine the imaging force during scanning. Owing to the oscillation motion of a tapping mode tip, the exact applied force between tip and sample surface intermittently changes within one tapping cycle and is difficult to be confirmed. However, imaging is performed while the amplitude is kept constant by feedback loop and the imaging force is directly correlated with tip amplitude, as mentioned above. Therefore, the average imaging force of amplitude modulated tapping mode AFM is also kept constant and can be obtained as

$$F(nN) = [FreeAmp(V) - Setpoint(V)] \times k(N/m) \times AmpInvOLS(nm/V) \quad (4\text{-}9)$$

where k is a spring constant of the cantilever and *AmpInvOLS* is the inverted optical lever sensitivity settings for converting an amplitude signal from V to nm, which can been calculated by amplitude-phase-distance (APD) curve measurement. APD curve measurement, where amplitude and phase signals are simultaneously recorded as the tip approaches towards and retracts from the sample surface. From equation (4-9), one can find that in order to decrease the average applied load during scanning the set-point amplitude should set to be close to the free amplitude. As to free amplitude, it has been expressed as a function of drive amplitude and drive frequency in a complex way, as shown in equation (4-3) and (4-7). Taken together, it is possible to modulate the applied force during tapping mode AFM by adjusting the corresponding scan parameters according to equation (4-9), such as set-point, drive amplitude, and drive frequency.

3-2. Determination of Energy Dissipation in Tapping Mode AFM

From the viewpoint of energy conservation, Cleveland *et al*. introduced a method to calculate the energy dissipated by tip-sample interaction in tapping mode AFM [6]. In equilibrium, the average rate at which energy is input into the cantilever must equal to the average rate at which energy is dissipated by the cantilever and the tip.

$$\overline{P}_{in} = \overline{P}_{tip} + \overline{P}_{med} \quad (4\text{-}10)$$

, where P_{med} can be thought of as background dissipation that is present, and P_{tip} is the tip and cantilever power dissipation during scanning. The total average power yields

$$P_{in} = k(z - z_d)\frac{dz_d}{dt} = \frac{1}{2}kA_dA\omega\sin\varphi \quad (4\text{-}11)$$

Assuming that the background dissipation is well modeled by viscous damping of the cantilever body in media, P_{med} can be obtained as

$$\overline{P}_{med} = \frac{1}{2}bA^2\omega^2 \quad (4\text{-}12)$$

Therefore, the average power dissipation per oscillation cycle is given by

$$\overline{P}_{tip} = \overline{P}_{in} - \overline{P}_{med} = \frac{1}{2}\frac{kA^2\omega}{Q}\left[\frac{QA_d\sin\varphi}{A} - \frac{\omega}{\omega_0}\right] = \frac{\pi kA^2 f}{Q}\left[\frac{Q\sin\varphi}{A/A_d} - \frac{\omega}{\omega_0}\right] \quad (4\text{-}13)$$

, where f denotes drive frequency $(\omega=2\pi f)$. According to the simultaneous equations, namely equations (4-3), (4-5), (4-6), (4-7) and (4-13), one can calculate the energy dissipation by utilizing the data derived from APD curve measurement.

A calculating example of energy dissipation in the case of changing drive amplitude is shown in Figure 4-4. The APD curve measurements in Figure 4-4 (a) clearly showed that with decreasing tip-sample distance, the amplitude monotonously decreased but the phase shift sharply decrease below 90 ° at a certain distance, which

indicates that the attribute of tip-sample force perform conversion from attractive to repulsive regime. Furthermore, large drive amplitude gave APD curves with almost no attractive regime. By calculating with equations above, energy dissipation can be easily obtained from APD curves, as shown in Figure 4-4 (b).

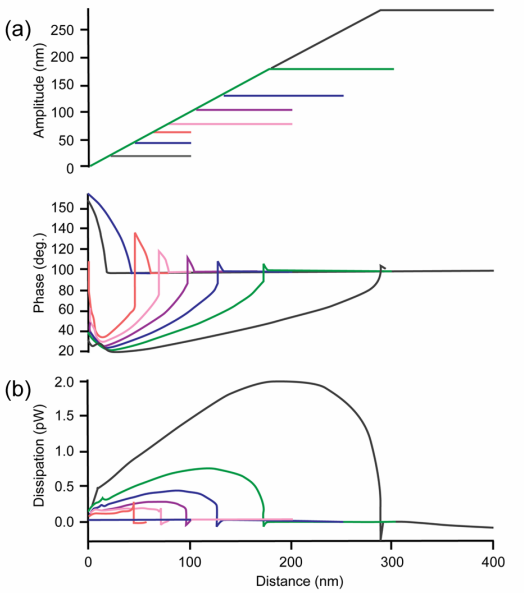

Figure 4-4. Amplitude, phase shift, and energy dissipation versus distance curves illustrating the dependence of the drive amplitude on tip-sample interaction.

4. Summary

In this chapter evaluation of tip-sample interaction in tapping mode AFM was established. Combined with the amplitude-phase-distance curve measurement, it is possible to calculate the average imaging force and the average power dissipation by the tip-sample interaction. As to soft matter observation with tapping mode AFM, it is reasonable to assume that the magnitude of deformation could be related to the magnitude of the tip-sample interaction, which will be discussed in Chapter 5.

References

1. G. Binnig *et al*., *PRL*, 1982, 49, 57.

2. G. Binnig *et al*., *PRL*, 1986, 56, 930.

3. M.E. McConney *et al*., *Polym. Rev.*, 2010, 50, 235.

4. R. Garcia *et al*., *Surf. Sci. Rep.*, 2002, 47, 197.

5. G. Bar *et al*., *Langmuir*, 1998, 14, 7343.

6. J. P. Cleveland *et al*., *Appl. Phys. Lett.*, 1998, 72, 2613.

Chapter 5

Controllable Deformation of Nanostructured Polymer Ultrathin Films with Atomic Force Microscopy

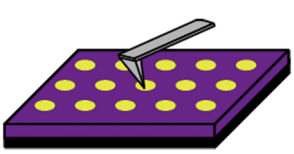

1. Introduction

Soft matter, such as polymer and biomacromolecules, are always rather compliant and soft. The distinct feature of soft matter is deformable and liquid-like. Typically, by continuously contacting with small AFM tip, sample surface will undergo permanent deformation.

In this chapter, the author demonstrated the correlation between the soft matter surface deformation and tip-sample interaction during AFM scanning. By altering the operation parameters, such as the set-point, drive amplitude, drive frequency and the number of scan, deformation of nanostructured polymer ultrathin film could be achieved in a controllable manner.

2. Construction of Polymer Ultrathin Films with Nanostructures

2-1. Routines for Film Preparing

The polymers used in this study were PS (Mw = 170,000; Mw/Mn = 1.06; d = 1.05 g/cm^3) and PMMA (Mw = 120,000; Mw/Mn = 1.8-2.0; d = 1.19 g/cm^3), which were purchased form Chemco Scientific Co., Ltd. (Osaka) and Sigma-Aldrich (St Louis, MO), respectively. The spin-casting substrates used in this study were silicon (100) wafers covered with 200 nm thermally grown silicon oxide (SiOx) purchased from KST World Co. (Fukui), which were cut into a size of 20 × 20 mm^2. The substrates were cleaned at 120°C in a piranha solution of sulfuric acid and 30% hydrogen peroxide (3:1, v/v) for 15 min and then thoroughly rinsed with deionized water (resistivity 18 MΩ cm) and dried with compressed nitrogen gas.

Polymer blend solutions were prepared by dissolving PS and PMMA with various weight ratios in analytical grade ethyl acetate as a common solvent. The mixture was

stirred overnight prior to film preparation in order to ensure complete dissolution. Unless otherwise stated, the total polymer concentration in the solutions was 1.0 wt%. The ultrathin polymer blend films were prepared by spin-casting at 5000 rpm for 60 s using a spin coater MS-A100 (MIKASA Co., Ltd., Tokyo). All routines for film preparation were conducted at room temperature (25°C) and normal relative humidity (~35% RH) in a clean room to avoid contamination. The schematic illustration of construction of polymer thin films with nanostructures can be found in Figure 5-1.

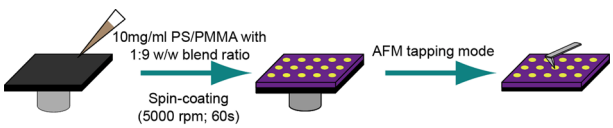

Figure 5-1. Illustration of construction of polymer thin films with nanostructures.

2-2. Atomic Force Microscopy for Ultrathin Films

The AFM used was a MFP-3D (Asylum Research, Santa Barbara, CA) at room temperature, controlled by software 0909091+1214 and Igor Pro 6.12A environment (WaveMetrics, Lake Oswego, OR).

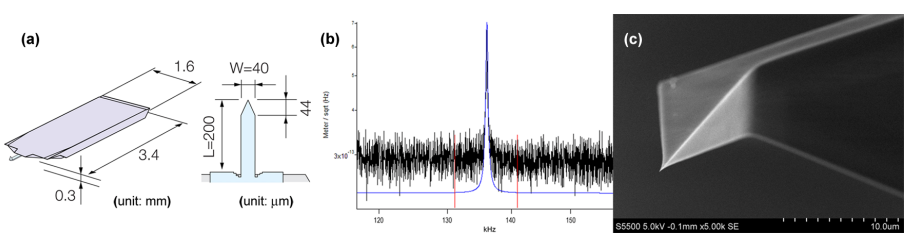

Figure 5-2. Calibration of the chosen silicon cantilever. (a) Dimensional size of the cantilever; (b) Thermal PSD result to show the resonance frequency of the cantilever; (c) SEM image of a fresh tip, taken by FE-SEM S-5500 (Hitachi High-Technologies, Tokyo).

Imaging was performed using a silicon cantilever AC200TS (Olympus, Tokyo) with scan size of 5 × 5μm^2 and scan speed of 25.04 μm/s. The dimensional size of this cantilever can be found in Figure 5-2 (a). Resonance frequency of cantilever was confirmed by thermal power spectral density (PSD) measurement to show a value of 136.156 kHz and spring constant was calibrated to be 7.5 N/m (Figure 5-2 (b)), which generally agrees with the nominal values (75-175 kHz and 4.0-22.3 N/m). The author used scanning electron microscopy (SEM) to check whether the tip is always in a good condition. The shape of tip was no significantly different before and after the usage, making evident that the chosen tip is hard enough to deform the polymer surface in this study (Figure 5-2 (c)).

2-3. Topographical Features of Ultrathin Films

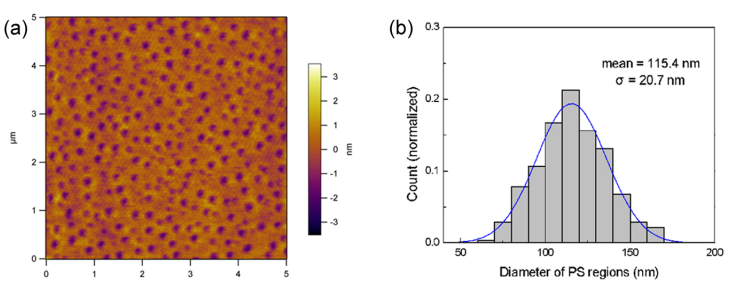

Figure 5-3. Topographical features of ultrathin films sample. (a) AFM height image after one time scan at light tapping. (b) Gaussian fitting (blue line) for diameter of PS regions exhibited in (a).

The thickness of a sample film was determined by scratching the sample with a scalpel and then measuring the lateral profile by AFM. It was found all the films are "ultrathin" with thickness of ~30 nm. The nanostructure exhibited on the film was statistically measured. The AFM images without observable plastic deformation were

chosen to be analyzed by using ImageJ (NIH, Bethesda, MD) software. Usually, these images taken at “light tapping”, namely the set-point amplitude closes to the free amplitude. At least ten AFM images were analyzed and averaged that the diameter of PS regions is ~110 nm. There is a calculating example shown in Figure 5-3.

3. Deformation Behavior of Ultrathin Films with Tapping Mode AFM

3-1. Effect of Number of Scans on Deformation Behavior

Herein, the author reports a study on the deformation of nanostructured polymer surface with tapping mode AFM, which has remained unexplored. As a preliminary experiment, PS homopolymer films with thickness of ~30 nm were prepared on silicon oxide substrate. The author intentionally operated AFM at large average imaging force of ~5 μN to enhance the tip-sample interaction. By repetitive scanning, ripple structures gradually appeared and developed on the surface of the PS film, which coincides with contact mode studies [1-6]. Although tapping mode AFM can minimize the applied load and essentially eliminate the lateral force, polymer surface deformation can still happen [7, 8]. It is confirmed that the results obtained in this study are comparable to the previous ones.

The author then prepared thin polymer ultrathin films with nanostructures by using PS/ PMMA blend phase separation. In a typical sample, morphological feature of an as-cast film will show numerous PS cylinders distributed in a matrix of PMMA (Figure 5-4 (a)). Height difference of PS and PMMA has been explained elsewhere [9]. Interestingly, by repetitive scanning, all of the PS regions were gradually deformed and ploughed out of the PMMA matrix, whereas PMMA matrix is completely stable and deformation-resistant (Figure 5-4 (b)). As number of scans increases, the amount of PS piled up increases (Figure 5-4 (c) and (d)), indicating that the deformation is a

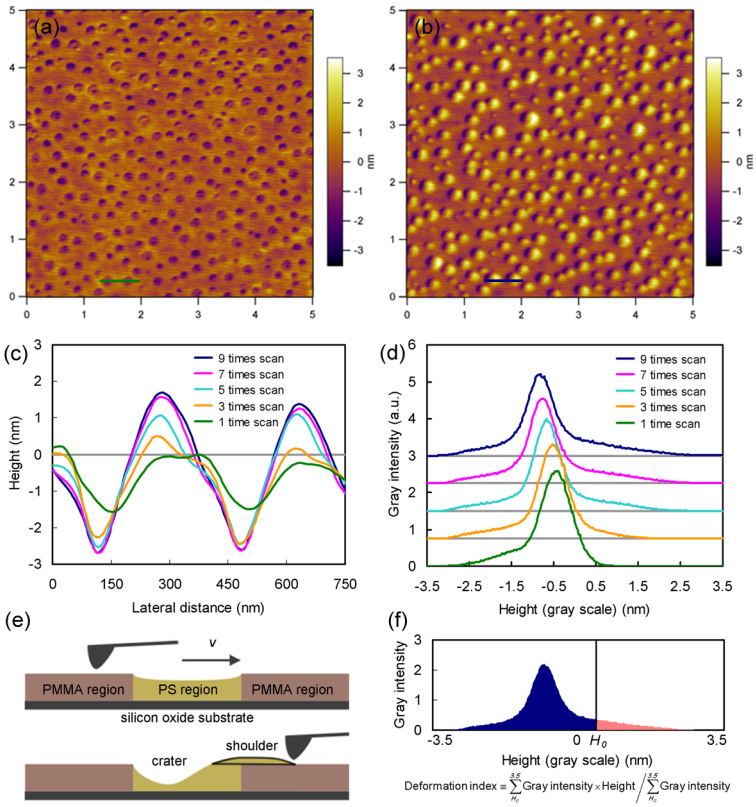

Figure 5-4. Number of scans induced surface deformation. (a) AFM image after one time scan. (b) *In situ* AFM image after nine times scans. (c) Lateral profile corresponding to the line shown in (a) and (b) for nine times scans. Green line shows a ~1.5 nm height difference between original PS and PMMA regions. (d) Gray histogram of each AFM image for nine times scans. (e) Cartoon of a tapping tip moved across nanostructured polymer surface and formation of "shoulder" and "crater" structure. (f) Definition of "deformation index", where H_0 refers to the top height of PMMA matrix. The gray histogram is an example and derived from (b). Height scale of all AFM images is set to be 7 nm, thus gray intensity can be deemed as an integral exhibition of height distribution of each image.

cumulative process like the formation of ripple structures. The asymmetry of the

resulting morphology possibly reflects the direction of tip motion during scanning (Figure 5-4 (e)). AFM images were never filtered in order to avoid possible artifacts and all the scan parameters can be found in Table 5-1.

Table 5-1. Summary of all the tapping mode AFM scan parameters used in this study.

Entry	Set-point (V)	Drive amplitude (mV)	Drive frequency (kHz)
Figure 5-4	1.5	400	136.5
Figure 5-6 (b)	0.5, 1.5, 2.5, 3.5, 4.5	400	137.0
Figure 5-6 (e)	2.5	600, 500, 400, 300, 200	137.0
Figure 5-6 (f)	2.0	400	136.0, 136.5, 137.0, 137.5, 138.0

While the mechanical properties of PS and PMMA are very similar in bulk [10], the deformation observed in this study is only limited to PS regions. Some reports showed that the apparent modulus of PS and PMMA decrease in the same manner that was below ~40 nm by using a buckling-based metrology [11, 12], as shown in Figure 5-5. The author applied this method and measured the Young's modulus of a serious of PS films with different thickness and found the similar results. However, such measurement required the film to be transferred onto a relatively soft and thick substrate, which could dramatically impact the confinement behavior and mechanical properties of thin polymer films.

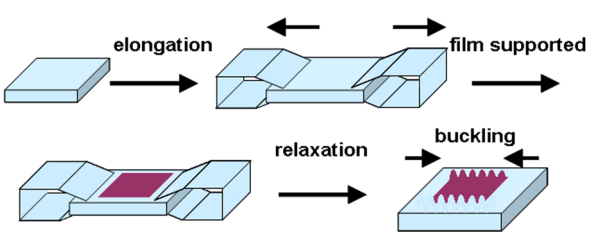

Figure 5-5. Illustration of strain-induced elastic buckling instability for mechanical measurement.

It has been widely reported that with decreasing film thickness below ~40 nm on silicon oxide substrate, the T_g of PS decreases, whereas *vice versa* for PMMA [13, 14]. The difference can be interpreted from the better interaction between PMMA chains and silicon oxide substrate compared to PS, which restrict the polymer mobility and increase the T_g. Previous report also showed that PMMA was very stable to AFM scan and no ripple structures were exhibited [15]. By using PS/PMMA blend thin film as a sample, our results supported these previous studies in a compelling way.

3-2. Effect of other Scan Parameters on Deformation Behavior

Now that the tip-sample interaction forms the origin of surface deformation, the author wondered if it is possible to construct the deformation by adjusting scan parameters, in stead of the number of scans. The author carefully changed the scan parameters, namely set-point (Figure 5-6 (b) and (d)), drive amplitude (Figure 5-6 (e) and (g)), and drive frequency (Figure 5-6 (f) and (h)) during imaging. In all cases, only one of these scan parameters was changed while the others were kept constant. Figure 5-6 clearly shows the validity of our strategy, which has proved surface deformation in a controllable manner. Combined with the result of repetitive scanning (Figure 5-6 (a) and (c)), it was found that the influence of each mentioned scan parameter on deformation is somewhat different, thus implying that different mechanism of deformations may occur simultaneously. For example, as set-point increases, the heights of both elevated PS and the inner PS regions increased (Figure 5-6 (b) and (d)). However, as drive amplitude increases, the amount of PS was piled up increasingly with the depressing of the inner PS regions (Figure 5-6 (e) and (g)).

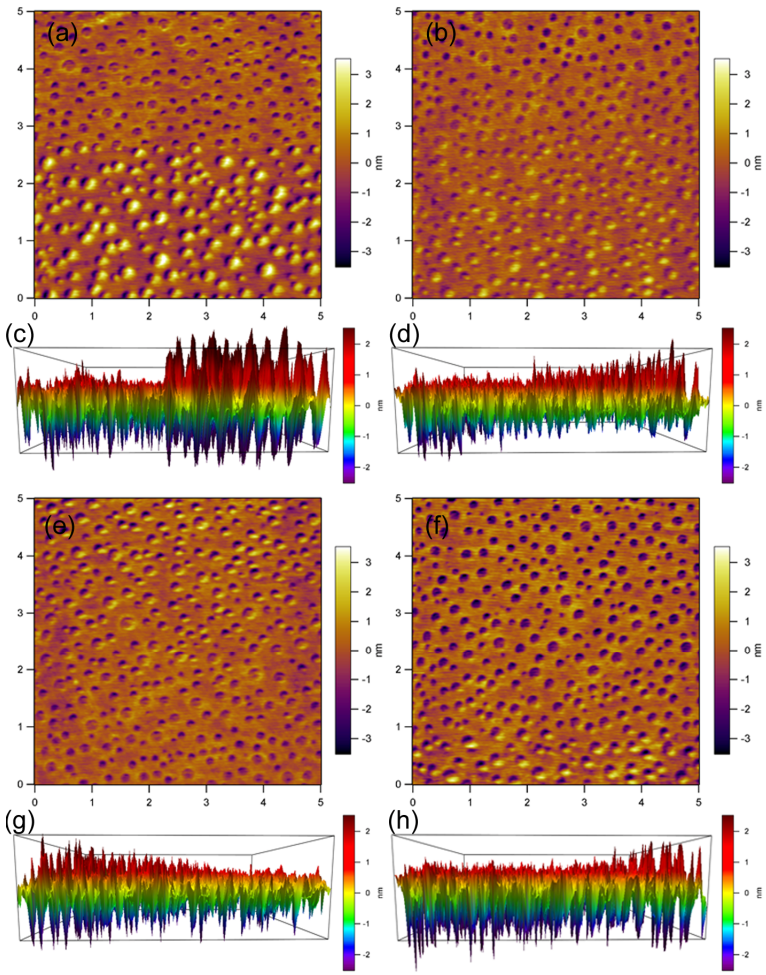

Figure 5-6. Surface deformation induced by a variety of scan parameters. (a) Number of scans influence. AFM can be equally divided to two parts from top to down, where shows morphology after one time scan and ten times scans. (b) Set-point influence. AFM image can be equally divided to five parts from top to down, where set-point was changed from 0.5 to 1.5, 2.5, 3.5, and 4.5 V. (e) Drive amplitude influence. AFM image can be equally divided to five parts from top to down, where drive amplitude was changed from 600 to 500, 400, 300, and 200 mV. (f) Drive frequency influence. AFM image can be equally divided to five parts from top to down, where drive frequency was changed from 136.0 to 136.5, 137.0, 137.5, and 138.0 kHz. (c), (d), (g), and (h) Cross section 3D images generated from (a), (b), (e), and (f), respectively.

4. Correlation of Deformation Behavior and Tip-Sample Interaction

4-1. Determination of Magnitude of Deformation Behavior

In comparison with featureless PS films, deformation of nanostructured PS/PMMA blend films was more complicated as compositional continuity was broken up by the geometric confinement. PMMA matrix restricted the formation of ripple structures, and hence PS is compelled to be ploughed out of the inner regions. According to Jones *et al*.'s model, the magnitude of deformation can be characterized by counting the amount of material at the periphery of the indentation (also called shoulder) [16]. As such, in order to describe the elevated deformation quantitatively, the average height of the PS shoulders is obtained by gray histogram of AFM image, referred as "deformation index" (Figure 5-4 (e) and (f)). All the results have been listed in Table 5-2. For example, in the case of repetitive scanning, the deformation index was found to increase from ~0.7 to ~1.3 nm after nine times scans. Obviously, the deformation observed at the shoulder regions is plastic deformation with observable amount of PS displaced. The author has verified that this deformation is permanent (at least for one month, data not shown) and the morphological feature of films does not return to its original one.

As to the depressed deformation of inner PS regions (also called crater), it is difficult to determine from AFM images. Despite of this, the tapping tip spends some time close to and in contact with the sample surface in each cycle of oscillation. Therefore, the indentation of tip into the soft sample cannot be neglected. The author measured the tip indentation on PS craters to describe the depressed deformation. For any given amplitude, the horizontal difference between the amplitude-distance curves of a soft and a stiff surface corresponds to the tip indentation [17, 18]. It is feasible to quantitatively determine the indentation of the tip into the soft PS regions by APD

measurement. A bare silicon substrate was used as a stiff surface. There is a calculating example in the case of changing set-point shown in Figure 5-7. In this study, the slope of amplitude-distance curve of PS regions is always smaller than that of silicon surface, indicating the PS vertically deformed by the interaction with a tapping tip. All the results have been listed in Table 5-2.

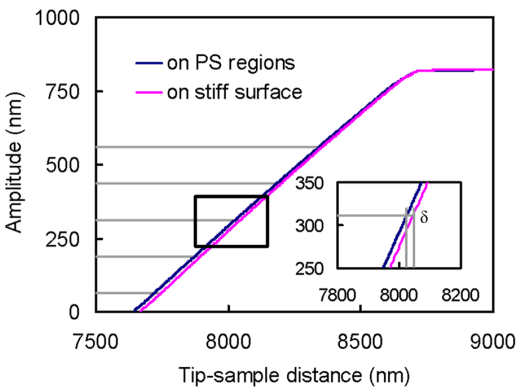

Figure 5-7. Amplitude-distance curves for nanoconfined PS region and stiff surface. At least 20 curves were recorded for each case and calculated as an average. Horizontal lines show set-point amplitude used in each case. Inset is a magnified view of the rectangle part as highlighted to show the determination of tip indentation, referred as δ.

It is found that the tip indentation can be applied in the range from ~5 to ~25 nm, which is much larger than the depth of PS crate observed from AFM image. The author reasoned that the elastic deformation appears to play an important role at the crater regions and most deformation is recovered immediately when tip retracts from surface. It is proposed that the depressed deformation observed from AFM image consists of two terms, an incomplete recovery of indentation of elastic deformation and a consequent hollow induced by PS displacement of plastic deformation.

Table 5-2. Results for determination of surface deformation and tip-sample interaction.

Entry	Indentation (nm)	Deformation index (nm)	Imaging force (μN)	Energy dissipataion (pW)
Figure 5-4	23.37	0.71, 0.96, 1.16, 1.26, 1.28	4.76	7.03, 21.09, 35.15, 49.21, 63.27
Figure 5-6 (b)	25.79, 22.23, 18.67, 15.11, 11.55	0.58, 0.81, 0.94, 1.01, 1.06	5.70, 4.77, 3.83, 2.90, 1.97	1.49, 9.38 18.30, 25.17, 26.79
Figure 5-6 (e)	21.05, 20.25, 16.82, 12.34, 6.19	1.24, 1.07, 0.95, 0.82, 0.69	4.57, 4.33, 3.83, 2.50, 0.95	47.54, 30.96, 18.30, 9.45, 4.65
Figure 5-6 (f)	18.76, 19.07, 19.83, 17.09, 5.11	0.76, 0.79, 0.85, 0.88, 1.03	4.30, 4.30, 4.30, 3.86, 0.82	6.24, 9.92 13.83, 16.73, 19.41

4-2. Correlation Analyses with Tip-Sample Interaction

In order to obtain a deeper understanding about the influences of scan parameters on surface deformation, APD curve measurement is carried out at PS regions, where amplitude and phase are recorded as the tip-sample distance is decreased. At least 20 APD curves were recorded for each case and calculated as an average (Figure 5-8 (a), (d), (g), and (j)). This study showed that the intentionally large drive amplitudes gave APD curves with almost no attractive regime and the minus phase shifts induced by tip-sample interactions indicated that the repulsive force dominated the scanning. The magnitude of average imaging forces are determined and found to be in the range from ~1 to ~6 μN (Figure 5-8 (b), (e), (h), and (k)). All the results have been listed in Table 5-2. Indentation and deformation index are plotted as a function of imaging force. It is found that the indentation is strongly proportional to the imaging force, whereas a poor correlation is obtained between deformation index and force (Figure 5-9 and Figure 5-10 (insert)).

As introduced in chapter 2, the local energy dissipation per oscillation cycle at PS regions can be calculated by using APD curves measurement. Results showed dissipation in this study could be adjusted in the range from ~1 to ~50 pW within one

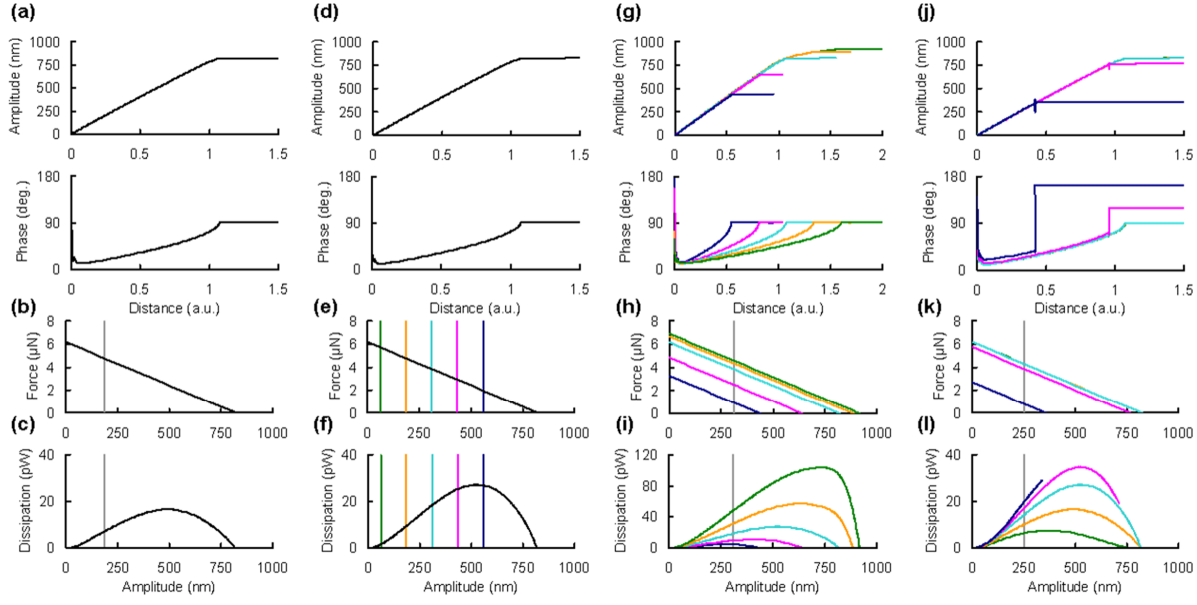

Figure 5-8. APD curve measurement and determination of tip-sample interaction. APD curve measurement (a), calculation of imaging force (b) and energy dissipation (c) versus set-point amplitude for changing number of scans. APD curve measurement (d), calculation of imaging force (e) and energy dissipation (f) versus set-point amplitude for changing set-point. Green: 0.5, orange: 1.5, cyan: 2.5, pink: 3.5 and blue: 4.5 V. APD curve measurement (g), calculation of imaging force (h) and energy dissipation (i) versus set-point amplitude for changing drive amplitude. Green: 600, orange: 500, cyan: 400, pink: 300 and blue: 200 mV. APD curve measurement (j), calculation of imaging force (k) and energy dissipation (l) versus set-point amplitude for changing drive frequency. Green: 136.0, orange: 136.5, cyan: 137.0, pink: 137.5 and blue: 138.0 kHz. Vertical lines in (b), (c), (e), (f), (h), (i), (k), and (l) show set-point amplitude used in each case.

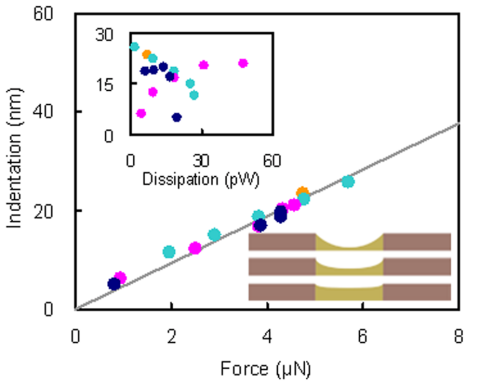

Figure 5-9. Tip indentation plotted as a function of imaging force and energy dissipation (insert). Cartoon shows a schematic view of elastic deformation of PS regions. Orange: results from repetitive scanning, cyan: results from changing set-point, pink: results from changing drive amplitude, and blue: results from changing drive frequency, all of which are displayed together.

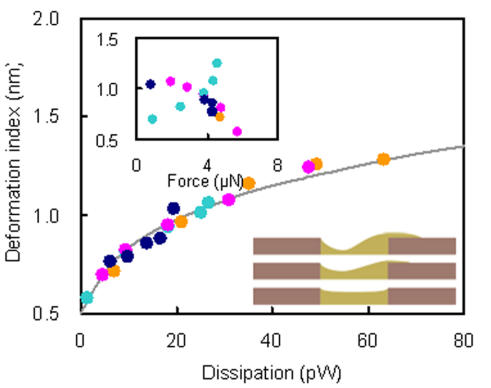

Figure 5-10. Deformation index plotted as a function of energy dissipation and imaging force (insert). Cartoon shows a schematic view of plastic deformation of PS regions. Orange: results from repetitive scanning, cyan: results from changing set-point, pink: results from changing drive amplitude, and blue: results from changing drive frequency, all of which are displayed together.

time scan (Figure 5-8 (c), (f), (i), and (l)). All the results have been listed in Table 5-2. The author plotted the indentation and deformation index as a function of energy dissipation. No correlation was found between indentation and energy dissipation,

whereas deformation index was strongly correlated with energy dissipation (Figure 5-9 (insert) and Figure 5-10). Results showed that the greater the energy released to the PS regions, the greater the amount of PS can be piled up, i.e., the severe case of the plastic deformation. Due to the volume of each inner PS region, the height of elevated PS ought to have a limitation, which can also be confirmed (Figure 5-10).

The plastic deformation of PS regions is a wear process in the presence of friction. Based on adhesive theory, lateral force is correlated with contact area, which is always proportional to applied load [19]. This had offered a reasonable explanation for the size of ripple structures increasing with applied load in contact mode studies. However, the results derived from tapping mode AFM has revealed a more complicated behavior of surface deformation and cannot be explained straightforwardly. The author has proved that applied force is indeed a key parameter to control the elastic deformation. As to plastic deformation, there is a multiplicity of influences observed in this study. For example, while applied force is large, small amplitude cannot give an observable shoulder structure (Figure 5-6 (d)), and *vice versa* (Figure 5-6 (g)). The author proved that all the scan parameters can be integrated into energy dissipation, which showed good correlation with plastic deformation of PS regions.

5. Summary

It is widely accepted that bulk plastic deformation is associated with energy dissipation. Here, the experimental study is the first to prove such relationship in nanoscale by using nanostructured polymer surface with tapping mode AFM. The energy lost in the tip-sample interaction (or at least portion of it) is the source of surface deformation. The results are of practical value in nanofabrication and significant to the stability of an actual nanodevice.

References

1. O.M. Leung *et al*., *Science*, 1992, 255, 64.

2. G.F. Meyers *et al*., *Langmuir*, 1992, 8, 2330.

3. R.H. Schmidt *et al*., *Langmuir*, 2003, 19, 898.

4. B.D. Beake *et al*., *Wear*, 2004, 256, 118.

5. B.D. Beake *et al*., *Polymer*, 2001, 42, 7025.

6. R.H. Schmidt *et al*., *Langmuir*, 2003, 19, 10390.

7. J. Tamayo *et al*., *Langmuir*, 1996, 12, 4430.

8. E. Thormann *et al*., *Ultramicroscopy*, 2010, 10, 313.

9. S. Walheim *et al*., *Macromolecules*, 1997, 30, 4995.

10. J. Brandrup *et al*., *Polymer Handbook*, Wiley Science, 1999.

11. C.M. Stafford *et al*., *Nat. Mater.*, 2004, 3, 545.

12. C.M. Stafford *et al*., *Macromolecules*, 2006, 39, 5095.

13. D.S. Fryer *et al*., *Macromolecules*, 2000, 33, 6439.

14. C.B. Roth *et al*., *Macromolecules*, 2007, 40, 2568.

15. J.B. Peng *et al*., *Thin Solid Films*, 1996, 284, 444.

16. F.N. Jones *et al*., *Prog. Org. Coat.*, 1998, 34, 119.

17. R. Hoper *et al*., *Ultramicroscopy*, 1995, 60, 17.

18. A. Knoll *et al*., *Macromolecules*, 2001, 34, 4159.

19. F.P. Bowden *et al*., *The Friction and Lubrication of Solids*, Oxford University Press, 2001.

Chapter 6

Conclusions and Future Prospects

1. Conclusions

2. Future Prospects

References

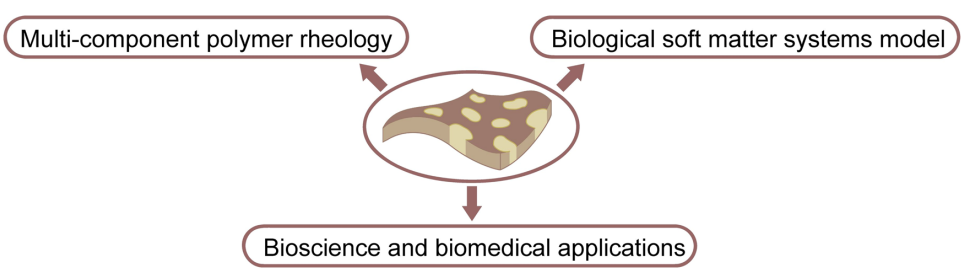

1. Conclusions

In this thesis, the author described a tentative exploration on construction of polymer ultrathin films with nanostructures as a model for biological soft matter systems. It is convinced that the methodology present here is an effective way to acquire various nanostructures. As a soft matter model, its deformation behavior is emphasized in the subsequent work. The primary conclusions were as follows:

1. Fundamental methodology to construct polymer ultrathin films with nanostructures was established by polymer blend phase separation. The author proposed a simple model for the phase separation mechanism within ultrathin films, indicating that the SD mechanism plays important role in determining the final morphology. (Chapter 2)

2. A series of simple and fast methods was developed and proven as a versatile way to prepare porous polymer ultrathin films with controllable pore size. Combined with freestanding technique, a potential use of porous ultrathin films in bioapplication, such as optical coating or biofilter membrane, was proposed and discussed. (Chapter 3)

3. Based on a theoretical study on dynamics of AFM tip motion, the author introduced a technique to evaluate the tip-sample interaction in tapping mode AFM. By using amplitude-phase-distance curve measurement, the average imaging force and the power dissipation by the tip-sample interaction can be easily calculated. (Chapter 4)

4. By systematically studying the deformation behavior of nanostrucured polymer ultrathin films with AFM, the author established a correlation between surface deformation and tip-sample interaction, and first proved that the plastic deformation at nanoscale is associated with energy dissipation in a controllable manner. (Chapter 5)

2. Future Prospects

Further work is necessary to apply our nanostructured polymer ultrathin film system for bioscience and bioapplication. As to potential uses in bioapplication, the well-controlled nanostructures obtained in this work will be applicable for construction of the building blocks for biodevice, such as optical coating or biofilter membrane. Herein the author described the further prospects for polymer science and bioscience below. It is convinced that the polymer ultrathin films with nanostructures would be an innovative experimental model for both theoretical research and practical bioapplications.

2-1. Anomalous Behaviors of Polymer by Geometric Confinement

The study of polymer confinement effect has become a huge topic in polymer science and condensed matter physics over the past decade. Thickness of polymer ultrathin films is comparable to the dimension of polymer chain. Since the mobility of polymer at vertical direction is a dramatically restrained, ultrathin film always shows anomalous behaviors that are not seen in the bulk. Inspired by these results, if polymer chains are restrained at two or three directions, namely a tube-like or a particle-like ultrasmall volume, it is reasonable to expect their more complex features and interesting behaviors are derived from polymer confinement effect (Figure 6-1).

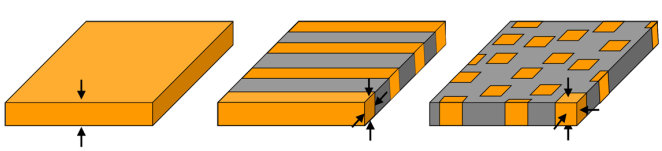

Figure 6-1. Illustration of one, two, and three directions geometric confinement of polymer within an ultrathin film (yellow: study polymer region, gray: matrix).

Conventional research on two or three dimensional confinement effect concentrate on molecular simulation and theoretical analyses, but experimental result is still very limit [1, 2]. The polymer ultrathin films with nanostructures constructed in this study are exactly able to provide a good experimental model for this issue, namely polymer can be restrained in tube-like or a particle-like ultrasmall volume, size of which is comparable to the dimension of polymer chain.

2-2. Lipid-Contained Polymer Ultrathin Films as Cell Membrane Model

One application of this study is to construct polymer ultrathin films that mimic the diversity of cell membrane, namely, a mechanically heterogeneous surface with a wide variety of nanostructures. The most commonly used cell membrane model is called black lipid membrane, where a bilayer is formed across an aperture on the Teflon sheet [3-5] (Figure 6-2). Typically the diameter of aperture is large as a few tens of micrometers, which makes black lipid membrane very fragile, short-lived and can be difficult to work with. Lipid-contained polymer ultrathin films are expected to overcome these barriers and develop a model to study the cell membrane behavior in a simply way.

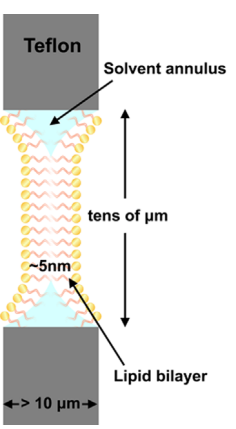

Figure 6-2. Illustration of black lipid membrane.

References

1. M. Alcoutlabi *et al*., *J. Phys.: Condens. Matter,* 2005, 17, R461.

2. K. Shin *et al*., *Nat. Mater.*, 2007, 6, 961.

3. M. Montal *et al*., *PNAS*, 1972, 69, 3561.

4. S.H. White *et al*., *Biophys. J.*, 1972, 12, 432.

5. H.T. Tien *et al*., *Planar Lipid Bilayers (BLM's) and Their Applications*, Elsevier Science, 2003.

Academic achievement

(List of Publications)

1. Hong Zhang, Shinji Takeoka. “Morphological Evolution within Spin-Cast Ultrathin Polymer Blend Films Clarified by a Freestanding Method”, *Macromolecules* 45, 4315 (2012).

2. Hong Zhang, Yukio Honda, Shinji Takeoka. “Controllable Deformation of Nanostructured Polymer Surface with Atomic Force Microscopy”, (submitted)

(International Symposium)

1. Hong Zhang, Shinji Takeoka. “Preparation of Freestanding Ultrathin Films with Uniform Nanopores by Polymer Phase Separation” *2nd Workshop for Diamond Researchers*, Tokyo, 2012.2

2. Hong Zhang, Shinji Takeoka. “Preparation of Nanoporous Freestanding Ultrathin Films by Polymer Blend Phase Separation” *243rd ACS National Meeting*, San Diego, 2012.3

(Patent)

1.「多孔質高分子超薄膜」, 特願 2012-54255

Acknowledgements

This thesis covers most of my work at the Department of Life Science and Medical Bioscience, Waseda University during 2009-2012. It has been written with the help, advice and moral support of many people. I must first thank my supervisor, Prof. Dr. Shinji Takeoka, for his continuous inspiration, valuable suggestions and trust in giving me the freedom to try my own ideas throughout this work. I also express my sincere gratitude to Prof. Dr. Yasuo Ikeda, Prof. Dr. Nobuhito Goda, and Prof. Dr. Shin'ichi Ishiwata for their efforts as members of the judging committee for this thesis. Many thanks to Prof. Yukio Honda in Consolidated Research Institute for Advanced Science and Medical Care, Waseda University, for sharing his expertise in experimental procedures. His attitude towards science inspired me to become a better researcher. I would also like to thank my previous supervisor, Prof. Dr. Fanglian Yao in Tianjin University, for her kind help when I move to Japan and moral support at all times.

I acknowledge to my mentor, Dr. Toshinori Fujie, for his kind encouragement at the beginning of this work. In addition, I owe considerable gratitude to Dr. Atsushi Murata, Mr. Akihiro Saito, Mr. Hiroki Haniuda, and Mr. Shota Hirosawa for their helpful advice and support during every process of my research. I would also like to express special thanks to my junior student, Miss. Natsuki Takamizawa, without her tremendous dedication and effort, I would not accomplish this work. My friends have made my life happy everyday and I would like to express my appreciation to them, Miss. Tianshu Li, Miss. Janet Suyun Tan, and Mr. Chen-Yu Hsieh. I really enjoyed our lunch time and interesting talks during the day. I apologize for not able to write down everyone’s name I have interacted with during the last three years in the lab, whose beautiful smiles will be forever in my heart.

My parents have always provided overwhelming support and I want them to know how grateful I am for their unconditional love and concerns. Finally I wish to thank my girl friend, Zhuzhu Li. Her love and kindness helped me to succeed during the difficult periods. I also appreciate many helpful discussions we have had for this thesis.

July, 2012

Hong Zhang